The sulfur solubility minimum and maximum in silicate melt

Ery C. Hughes: Te Pū Ao | GNS Science (e.hughes@gns.cri.nz)
Lee Saper: Caltech (lsaper@caltech.edu)
Philippa Liggins: University of Cambridge (pkl28@cam.ac.uk)
Edward M. Stolper: Caltech (ems@caltech.edu)

This paper is a non-peer review pre-print submitted to EarthArXiv, which has been submitted to the Journal of the Geological Society thematic collection on Sulfur in the Earth System for peer review.

Twitter handles: @eryhughes, @lsaper, @pip_liggins

Abstract

The behaviour of sulfur in magmas is complex because it dissolves as both sulfide (S^{2-}) and sulfate (S^{6+}) in silicate melt. An interesting aspect in the behaviour of sulfur is the solubility minima (SS^{min}) and maxima (SS^{max}) with varying oxygen fugacity (f_{O2}). We use a simple ternary model (silicate–S_2–O_2) to explore the varying f_{O2} paths where these phenomena occur. Both SS^{min} and SS^{max} occur when S^{2-} and S^{6+} are present in the silicate melt in similar quantities due to the differing solubility mechanism of these species. At constant T, a minimum in dissolved total S content (w^m_{ST}) in vapour-saturated silicate melt occurs along paths of increasing f_{O2} and either constant f_{S2} or P; for paths on which w^m_{ST} is held constant with increasing f_{O2}, the SS^{min} is expressed as a maximum in P. However, the SS^{min} is not encountered during closed-system depressurisation in the simple system we modelled. The SS^{max} occurs when the silicate melt is multiply-saturated with vapour, sulfide melt, and anhydrite. The SS^{min} and SS^{max} influence processes throughout the magmatic system, such as mantle melting, magma mixing and degassing, and SO_2 emissions; and calculations of the pressures of vapour-saturation, f_{O2}, and SO_2 emissions using melt inclusions.

Supplementary material: Additional information and data used to create the figures are included with the submission of this manuscript. The code used to generate the data is available at https://github.com/eryhughes/SSminmax.

It is widely accepted that there is a minimum in the solubility of sulfur (abbreviated to the SS^{min}, for the "sulfur solubility minimum") in silicate melts (i.e., in the concentration of dissolved S in a silicate melt coexisting with an S-bearing vapour) as a function of oxygen fugacity (f_{O2}) when the speciation of S in the silicate melt changes from being sulfide (S^{2-}) to sulfate (SO_4^{2-} or abbreviated as S^{6+}) dominated. This is based on experimental studies of the concentration of S in vapour-saturated silicate melts spanning a range in f_{O2} (e.g., Fincham and Richardson 1954; Katsura and Nagashima 1974; Carroll and Rutherford 1985; Backnaes and Deubener 2011; Lesne *et al.* 2015; Matjuschkin *et al.* 2016; Nash *et al.* 2019). Such a minimum in S solubility has implications for magmatic and volcanic processes. For example, any process where f_{O2} progressively changes and becomes closer to the f_{O2} of SS^{min} (e.g., mixing, progressive reduction or oxidation, degassing etc.) will result in a decrease in the S-solubility. This minimum has been used as evidence of the presence of additional, low solubility, potentially unquenchable, S-bearing species in silicate melts that could be important for metal transport in arc systems (Matjuschkin *et al.* 2016). Also, understanding the thermodynamic basis for this feature is critical for calculating the pressure of vapour-saturation of S-bearing magmas using the volatile concentrations of quenched glasses (e.g., Lesne et al., 2015).

Despite its potential importance, the existence of an SS^{min} with varying f_{O2} has been somewhat mischaracterised in the literature. As emphasized by O'Neill (2020), this is at least in part due to a lack of clarity regarding the independent variables and the path followed by sulfur fugacity (f_{S2}) with increasing f_{O2} for specific natural or experimental processes (e.g., Moretti et al., 2003) and the number and identity of additional S-bearing phase(s) with which the silicate melt is saturated (e.g., Jugo et al., 2005). In this paper, we explore the conditions and paths for which an SS^{min} occurs and some of the implications for magmatic and volcanic processes. We also expand upon the work of Jugo (2009) regarding a S solubility *maximum* (referred to as an SS^{max}) for silicate melts that are multiply saturated with sulfide melt + anhydrite ± vapour. We note that although silicate melt and vapour in most natural systems contain H, C, halogens, metals, etc., in addition to S and O; here, we limit ourselves to a simple system in which S and O are the only volatile components in the silicate melt (although such a system may be appropriate of Jupiter's moon Io: e.g., Zolotov and Fegley, 2000). By limiting our treatment to this simple end-member system, the factors leading to an SS^{min} or an SS^{max} can be more easily isolated and understood.

Thermodynamic modelling

Equilibria between silicate melt, vapour, sulfide melt, and anhydrite

Sulfur occurs in several phases in magmatic systems, including dissolved S-bearing species in silicate melt, gaseous species in vapour, immiscible sulfide melts, and various sulfate phases (e.g., reviews by Parat et al., 2011; Wallace and Edmonds, 2011). In addition to silicate melt and vapour, we consider pure Fe-sulfide melt (FeS) and anhydrite ($CaSO_4$) (Figure 1a and b). The silicate melt end member can be compositionally simple (e.g., SiO_2, $CaMgSi_2O_6$, $NaAlSi_3O_8$) or complex (e.g., a natural basalt), provided it is fixed in composition. In our calculations, the silicate component is taken to be a S-free Hawaiian basaltic melt in which all the Fe is present as Fe^{2+} (composition given in the Supplementary Material). We assume that the silicate melt is insoluble in the vapour.

The vapour is assumed to be constrained to the S–O binary subsystem and to contain only three species (S_2, O_2, and SO_2; Figure 1b), hence

$$x^{v}_{S2} + x^{v}_{O2} + x^{v}_{SO2} = 1, \quad (1)$$

where x^{v}_{i} is the mole fraction of species *i* in the vapour. Other species are present in an S–O vapour (e.g., SO_3, SO, S polymers, etc.) and could be added to our treatment. However, the three species in equation (1) are the most significant (e.g., Oppenheimer *et al.* 2011; Renggli *et al.* 2017; Henley and Seward 2018; Henley and Fischer 2021) and are sufficient to illustrate the salient points.

Sulfide (S^{2-}) and sulfate (S^{6+}) are assumed to be the only significant S-bearing species dissolved in natural silicate melts based on XANES measurements and solubility experiments (e.g., Fincham and Richardson 1954; Paris *et al.* 2001; Métrich *et al.* 2009; Wilke *et al.* 2011). Intermediate S-bearing species have been observed or inferred (e.g., S^{4+}, $S_3^{\cdot-}$, S^0, molecular SO_2: Clemente *et al.* 2004; Métrich and Wallace 2009; Burgisser *et al.* 2015; Lesne *et al.* 2015; Matjuschkin *et al.* 2016; Colin *et al.* 2020), but these species are not thought to be significant in natural (especially in Fe-bearing) silicate melts. Hence, the silicate melt is assumed to contain only two S-bearing species (S^{2-} and S^{6+}; Figure 1b), such that

$$w^{m}_{S2-} + w^{m}_{S6+} = w^{m}_{ST}, \quad (2)$$

where w^{m}_{i} is the weight fraction of species *i* in the silicate melt, and S_T refers to total dissolved S content.

Three independent reactions control the coexisting compositions of silicate melt and vapour in this system. The first reaction describes a homogeneous equilibrium that governs the speciation of the vapour (*v*):

$$0.5S_2(v) + O_2(v) = SO_2(v), \quad (3a)$$

which is governed at equilibrium by

$$K_3(T) = \frac{f_{SO_2}}{(f_{S_2})^{0.5} f_{O_2}}, \quad (3b)$$

where K_3 is the equilibrium constant for reaction (3a) and f_i is the fugacity of species *i* in the vapour. If the treatment were to include other S ± O-bearing vapour species (such as SO_3, SO, etc.; see above), a statement of homogeneous equilibrium would have to be added for each additional vapour species.

The second reaction describes a heterogeneous equilibrium between silicate melt (*m*) and vapour that governs the dissolution of sulfur from the vapour as S^{2-} in the silicate melt (e.g., Fincham and Richardson 1954; Moretti and Ottonello 2005, 2003; Moretti and Papale 2004; Gaillard and Scaillet 2009, 2014; Baker and Moretti 2011; Gaillard *et al.* 2011, 2013, 2015; Baumgartner *et al.* 2017; Moretti 2021), described by the following three relations:

$$0.5S_2(v) + O^{2-}(m) = 0.5O_2(v) + S^{2-}(m), \quad (4a)$$

$$K_4(P,T) = \frac{a^{m}_{S2-}}{a^{m}_{O2-}}\left(\frac{f_{O_2}}{f_{S_2}}\right)^{0.5} \approx \frac{x^{m}_{S2-}}{x^{m}_{O2-}}\left(\frac{f_{O_2}}{f_{S_2}}\right)^{0.5}, \text{ and} \quad (4b)$$

$$C_{S2-} = w^m_{S2-}\left(\frac{f_{O_2}}{f_{S_2}}\right)^{0.5}; \quad (4c)$$

where a^m_i, x^m_i, and w^m_i are the activity, mole fraction, and weight fraction, respectively, in the silicate melt of the i^{th} ion (either S^{2-} or oxide [O^{2-}], in this case); and C_{S2-} is referred to as the sulfide capacity (e.g., Fincham and Richardson 1954; O'Neill 2020). The final term of equation (4b) makes the approximation that a^m_i can be replaced by x^m_i, and this approximation is adopted throughout. Given this approximation, C_{S2-} is simply related to K_4, the equilibrium constant for reaction (4a), but by convention it is defined in terms of w^m_i rather than x^m_i. Finally, we assume throughout that x^m_{O2-} (i.e., the O^{2-} that is part of the silicate melt that can be replaced by S^{2-}) can be approximated as constant (i.e., $x^m_{S2-} << x^m_{O2-}$).

A third reaction describes an additional heterogeneous equilibrium between silicate melt and vapour that governs the dissolution of sulfur from the vapour as SO_4^{2-} in the silicate melt (e.g., Fincham and Richardson 1954; Moretti and Ottonello 2003, 2005; Moretti and Papale 2004; Baker and Moretti 2011; Moretti 2021):

$$0.5S_2(v) + 1.5O_2(v) + O^{2-}(m) = SO_4^{2-}(m), \quad (5a)$$

$$K_5(P,T) = \frac{a^m_{S6+}}{a^m_{O2-}\left(f_{S_2}{f_{O_2}}^3\right)^{0.5}} \approx \frac{x^m_{S6+}}{x^m_{O2-}\left(f_{S_2}{f_{O_2}}^3\right)^{0.5}}, \text{ and} \quad (5b)$$

$$C_{S6+} = w^m_{S6+}\left(f_{S_2}{f_{O_2}}^3\right)^{-0.5}; \quad (5c)$$

where a^m_{S6+} and x^m_{S6+} are the activity and mole fraction, respectively, of sulfate dissolved in the silicate melt; and C_{S6+} is referred to as the sulfate capacity (Fincham and Richardson 1954). Again, C_{S6+} is simply related to K_5, the equilibrium constant for reaction (5a), but using weight fraction instead of mole fraction, and assuming x^m_{O2-} is constant.

An alternative heterogeneous equilibrium between silicate melt and vapour can be used instead of either reaction (4a) or (5a) to describe the conversion of S^{2-} to S^{6+} in the silicate melt (e.g., Wallace and Carmichael 1994; Matthews *et al.* 1999; Métrich *et al.* 2009; Jugo *et al.* 2010; Baumgartner *et al.* 2017):

$$S^{2-}(m) + 2O_2(v) = SO_4^{2-}(m), \quad (6a)$$

$$K_6(P,T) = \frac{a^m_{S6+}}{a^m_{S2-}\left(f_{O_2}\right)^2} \approx \frac{x^m_{S6+}}{x^m_{S2-}\left(f_{O_2}\right)^2}, \text{ and} \quad (6b)$$

$$\frac{x^m_{S6+}}{x^m_{S2-}} = \left[\frac{S^{6+}}{S^{2-}}\right]^m = \frac{w^m_{S6+}}{w^m_{S2-}} = \frac{C_{S6+}}{C_{S2-}}f^2_{O_2}. \quad (6c)$$

Reaction (6a) can be obtained by subtracting reaction (4a) from reaction (5a) and rearranging. Reaction (6a) is useful as it emphasizes that the oxidation state of S dissolved in the silicate melt (i.e., $[S^{6+}/S^{2-}]^m$ or $[S^{6+}/S_T]^m$) at a given T and P is controlled only by f_{O2}, C_{S2-}, and C_{S6+}. However, C_{S2-} and C_{S6+} are highly dependent on the composition of the silicate melt (e.g., O'Neill and Mavrogenes 2002, 2019; Moretti and Ottonello 2005; Nash *et al.* 2019; O'Neill 2020; Boulliung and Wood 2021; Moretti 2021). Additionally, they will depend on T and P (because K_4 and K_5

must depend on T and P unless the standard state enthalpy and volume changes of the reactions are zero) and are likely to depend on the speciation of other multivalent elements in the silicate melt (e.g., $[Fe^{3+}/Fe^{2+}]^m$). Although such factors could lead indirectly to variations in $[S^{6+}/S^{2-}]^m$ at constant f_{O2}, these are expected to be minor effects for most for the examples considered here. Therefore, we assume C_{S2-} and C_{S6+} depend only on T and the composition of the silicate component (and depend only on total Fe not $[Fe^{3+}/Fe^{2+}]^m$), all of which are constant in all our calculations.

Given equation (1), if an S–O vapour is present in the system (i.e., if the silicate melt is vapour-saturated), the sum of the partial pressures (p_i) of the species in the vapour equals the total pressure of the system (P):

$$P = p_{O2} + p_{S2} + p_{SO2}, \tag{7}$$

where the partial pressures are related to fugacity and mole fraction in the vapour through fugacity coefficients (γ_i):

$$f_i = \gamma_i p_i = \gamma_i x^v_i P. \tag{8}$$

When the silicate melt is saturated with sulfide melt, the chemical potential of FeS in the silicate melt (μ^m_{FeS}) and the sulfide melt are equal. The "sulfide content at sulfide-saturation" (S^{2-}CSS) is the dissolved S^{2-} concentration in the silicate melt in equilibrium with sulfide melt (e.g., Shima and Naldrett 1975; O'Neill and Mavrogenes 2002; Smythe *et al.* 2017; O'Neill 2020):

$$w^m_{S2-} = w^m_{S2\text{-}CSS}. \tag{9}$$

The total S content of a silicate melt that is saturated with sulfide melt (S_TCSS) is then given by equation (9) in combination with equations (2) and (6c):

$$w^m_{ST} = w^m_{STCSS} = (1 + (C_{S6+}/C_{S2-})(f_{O2})^2) w^m_{S2\text{-}CSS}. \tag{10}$$

Alternatively, when the silicate melt is saturated with anhydrite, the chemical potential of $CaSO_4$ in the silicate melt (μ^m_{CaSO4}) and anhydrite are equal. The "sulfate content at anhydrite-saturation" (S^{6+}CAS) is the dissolved S^{6+} concentration in the silicate melt in equilibrium with anhydrite (e.g., Baker and Moretti 2011; Chowdhury and Dasgupta 2019; Zajacz and Tsay 2019):

$$w^m_{S6+} = w^m_{S6+CAS}. \tag{11}$$

The total S content of a silicate melt that is saturated with anhydrite (S_TCAS) is then given by equation (11) in combination with equations (2) and (6c):

$$w^m_{ST} = w^m_{STCAS} = (1 + (C_{S2-}/C_{S6+})(f_{O2})^{-2}) w^m_{S6+CAS}. \tag{12}$$

<u>The importance of the phase rule in our treatment of S-solubility in silicate melt</u>

In its simplest form, the phase rule relates the number of components (c) and phases (φ) in a system to the variance (or the degrees of freedom, F) of the assemblage:

$$F = c + 2 - \varphi. \quad (13)$$

For most of the calculations presented here, our system has three components (silicate, S_2, and O_2; $c = 3$) and two phases (silicate melt + vapour; $\varphi = 2$) (Figure 1a). This silicate melt + vapour assemblage is thus trivariant ($\varphi = 2$, $F = 3$); if only silicate melt were present, the system would be quadrivariant ($\varphi = 1$, $F = 4$). Therefore, for the silicate melt + vapour assemblage, if any three linearly independent intensive variables are chosen as independent variables, the state of the system is fully defined, and all other intensive variables are dependent. Consequently, the values of three independent variables *must* be given to completely specify the state of the system. The values of the other intensive variables can be calculated given the values chosen for the independent variables and knowledge of the thermochemistry of the silicate melt and vapour phases. Again, for vapour-undersaturated silicate melt, only one phase is present and four independent intensive variables are needed to define fully the state of the system.

The important point here is a restatement of the cautionary note in O'Neill (2020) about the SS^{min} when f_{O2} is an independent variable: i.e., assuming temperature (T) is constant, the variation of w^m_{ST} is *not* uniquely defined if only f_{O2} is independently varied. The behaviour of a third variable must also be specified for the state of the silicate melt + vapour assemblage to be defined at each point on a path of varying f_{O2}. Only then can the variation in w^m_{ST} (including the nature of any minimum or maximum) as a function of f_{O2} be uniquely characterized.

There are a variety of intensive variables that could be chosen as independent or dependent variables in our model system. For example, temperature (T); pressure (P); the dissolved S^{2-}, S^{6+}, and S_T content of the silicate melt, specified as x^m_i or w^m_i (given equation (2), only two of these three quantities can be chosen as independent variables); the bulk composition of the silicate melt, vapour, or the system as a whole, given as the mole or weight fractions of S, O, and/or silicate in the silicate melt, vapour, or system; or O_2, S_2, or SO_2 in the vapour (in either case these three variables must add up to one, so only two can be specified independently); the chemical potentials of all but one of the vapour species (μ^v_i, or equivalently fugacities, f_i, where $i = O_2$, S_2, or SO_2); the chemical potential of FeS and/or $CaSO_4$ in the silicate melt (μ^m_i) or in the coexisting sulfide melt and/or anhydrite if they are present; or the oxidation state of Fe and/or S in the silicate melt, (either $[Fe^{3+}/Fe^{2+}]^m$ or $[Fe^{3+}/Fe_T]^m$ and/or $[S^{6+}/S^{2-}]^m$ or $[S^{6+}/S_T]^m$), which is equivalent to specifying f_{O2}.

The composition of the silicate melt and vapour phases are described by our idealised three-component system. Although the compositions of the sulfide melt and anhydrite phases could be incorporated into our treatment, their compositions fall outside of the plane of our chosen three-component system. This means the composition of the silicate melt does not vary if sulfide melt and/or anhydrite phases are saturated in our calculations (i.e., Fe and Ca concentrations in the silicate melt are constant). Despite this, we can still model the effects of sulfide melt- and anhydrite-saturation on the properties of the silicate melt and vapour phases using μ^m_{FeS} or μ^m_{CaSO4} as described in "Silicate melt + (vapour and/or sulfide melt and/or anhydrite)Silicate melt + vapour + (sulfide melt and/or anhydrite)".

We use this conceptual background to explore trends in, and interrelationships among, various choices of independent and dependent variables, focussing on the implications for the SS^{min} and the SS^{max}. We model the silicate melt as a Hawaiian basalt; its composition and details of our choices of thermodynamic parameters for vapour and silicate melt can be found in the

Supplementary Material. For all of our calculations, T and the composition of the silicate component are held constant. Since we assume that $C_{S^{2-}}$ and $C_{S^{6+}}$ depend only on T and the composition of the silicate component, both of these parameters are the same in all calculations presented here. In particular, $C_{S^{2-}}$ and $C_{S^{6+}}$ are independent of P and $[Fe^{3+}/Fe_T]^m$, and therefore f_{O_2}. It is important to emphasize that the results based on our chosen parameters only describe the representative behaviour of the particular Hawaiian melt composition given in the Supplementary Material. Although we are confident that the trends and insights derived from this choice are robust, the exact behaviour depends strongly on the chosen values of $C_{S^{2-}}$ and $C_{S^{6+}}$. Therefore, the specific values of various variables – including the precise values of f_{O_2} where shifts in behaviour are predicted to occur – will likely vary strongly with T, composition of the silicate component, and the $C_{S^{2-}}$ and $C_{S^{6+}}$ parameterisation used (e.g., O'Neill and Mavrogenes 2002, 2019; Moretti and Ottonello 2005; Nash *et al.* 2019; O'Neill 2020; Boulliung and Wood 2021; Moretti 2021).

Independent variables of T, f_{O_2}, f_{S_2}, w^m_{ST}, P, μ_{FeS}, and μ_{CaSO_4}

In this section we calculate the state of the system by choosing T (1200°C) and a value of f_{O_2} ($-5 < \Delta FMQ < +5$, where FMQ is the Fayalite-Magnetite-Quartz buffer; FMβQ in Frost, 1991) as two of the independent variables. The other independent variables considered are f_{S_2}, w^m_{ST}, P, μ_{FeS}, and μ_{CaSO_4}. For any given state of the system (i.e., where the values of all intensive variables are defined), the results will be the same if any three variables are chosen as independent. Therefore, the following figures convey the same results, but with different variables as the axes and contours. For most of the P range shown in the following figures, $\gamma_i \sim 1$, hence $f_i \sim p_i$ using equation (8) (e.g., for $\log_{10}[P, \text{bar}] < 3$, $\gamma_i < 1.25$ for all species). "Silicate melt + vapour" describes the two-phase silicate melt + vapour assemblages, whilst "Silicate melt + vapour + (sulfide melt and/or anhydrite)" and "Silicate melt + (vapour and/or sulfide melt and/or anhydrite)" describe the silicate melt + (vapour and/or sulfide melt and/or anhydrite) assemblages. If the S content of the silicate melt is less than w^m_{ST} at vapour- and/or sulfide melt- and/or anhydrite-saturation, silicate melt is the only stable phase present.

Silicate melt + vapour

For silicate melt + vapour assemblages, $\varphi = 2$ and $F = 3$; therefore, in addition to T and f_{O_2}, only one other independent variable is needed to specify fully the state of the system. This third independent variable will be referred to as the "Y" variable: we first choose $Y = f_{S_2}$, then $Y = w^m_{ST}$, and finally $Y = P$. For each of these choices of the independent variables, we solve the system of equations (3b), (7), (8), and two out of (4c), (5c), and (6c).

S speciation in the silicate melt and vapour

silm, silicate melt; v, vapour; $sulf^m$, sulfide melt; anh, anhydrite; P^v_{sat}, pressure of vapour-saturation; f_{O_2}, oxygen fugacity; w^m_{ST}, total dissolved S content of the silicate melt.

Figure 2 shows how the compositions of the silicate melt and vapour change with varying f_{O_2} at constant T and either constant f_{S_2} (silm, silicate melt; v, vapour; $sulf^m$, sulfide melt; anh, anhydrite; P^v_{sat}, pressure of vapour-saturation; f_{O_2}, oxygen fugacity; w^m_{ST}, total dissolved S content of the silicate melt.

Figure 2a–b), constant w^m_{ST} (silm, silicate melt; v, vapour; sulf^m, sulfide melt; anh, anhydrite; P^v_{sat}, pressure of vapour-saturation; f_{O2}, oxygen fugacity; w^m_{ST}, total dissolved S content of the silicate melt.

Figure 2c–d), or constant P (silm, silicate melt; v, vapour; sulf^m, sulfide melt; anh, anhydrite; P^v_{sat}, pressure of vapour-saturation; f_{O2}, oxygen fugacity; w^m_{ST}, total dissolved S content of the silicate melt.

Figure 2e–f) given that the silicate melt is vapour-saturated. As f_{O2} changes, the speciation of sulfur in the silicate melt ($[S^{6+}/S_T]^m$) and in the vapour (x^v_{SO2}) change. This leads to changes with f_{O2} in the dominant species (or multiple species) in the silicate melt and vapour, which is indicated by the vertical background colour bands in silm, silicate melt; v, vapour; sulf^m, sulfide melt; anh, anhydrite; P^v_{sat}, pressure of vapour-saturation; f_{O2}, oxygen fugacity; w^m_{ST}, total dissolved S content of the silicate melt.

Figure 2. For the vapour, S_2 is the dominant species at low f_{O2} ($x^v_{SO2} < 0.1$, purple); SO_2 is the dominant species at high f_{O2} ($x^v_{SO2} > 0.9$, turquoise-green-yellow); and in between there is a transition from dominantly S_2 to SO_2 ($0.1 \leq x^v_{SO2} \leq 0.9$, blue). At sufficiently high f_{O2}, O_2 becomes more abundant than S_2 in the vapour (i.e., to the right of the point labelled α in the yellow band in silm, silicate melt; v, vapour; sulf^m, sulfide melt; anh, anhydrite; P^v_{sat}, pressure of vapour-saturation; f_{O2}, oxygen fugacity; w^m_{ST}, total dissolved S content of the silicate melt.

Figure 2b, d, and f), but both are much less abundant than SO_2 in the range shown. For the silicate melt, S^{2-} is the dominant S-bearing species at low f_{O2} ($[S^{6+}/S_T]^m < 0.1$, purple-blue-turquoise); S^{6+} is dominant at high f_{O2} ($[S^{6+}/S_T]^m > 0.9$, yellow); and in between it transitions from dominantly S^{2-} to S^{6+} ($0.1 \leq [S^{6+}/S_T]^m \leq 0.9$, green).

At constant T, the effects of varying the third independent variable ($Y = f_{S2}$, w^m_{ST}, or P) in addition to f_{O2} on the dependent variables (which are referred to as "Z" variables) are shown using contour plots in Figure 3–Figure 5. The coloured regions from silm, silicate melt; v, vapour; sulf^m, sulfide melt; anh, anhydrite; P^v_{sat}, pressure of vapour-saturation; f_{O2}, oxygen fugacity; w^m_{ST}, total dissolved S content of the silicate melt.

Figure 2 showing the dominant silicate melt and vapour species and their changes are also shown in Figure 3–Figure 5 using the same colour scheme. These regions in Figure 3–Figure 5 are separated by black curves, where dashed curves indicate isopleths of vapour speciation (x^v_{SO2} = 0.1 and 0.9) and solid curves indicate isopleths of silicate melt speciation ($[S^{6+}/S_T]^m$ = 0.1 and 0.9). Comparison of panels (d) in Figure 3–Figure 5 shows that the topology of the silicate melt and vapour speciation (indicated by the coloured fields) is similar for all three of these choices of Y.

A key point of Figure 3–Figure 5d is that regardless of the choice of the Y variable, at low f_{O2} ($\Delta FMQ \lesssim +0.7$) nearly all dissolved S is present as S^{2-} (purple-blue-turquoise). Under these conditions $w^m_{ST} \cong w^m_{S2-}$, and w^m_{ST} is controlled by equation (4c), giving w^m_{S2-} as a simple function of f_{O2} and f_{S2}. Likewise, at sufficiently high f_{O2} ($\Delta FMQ \gtrsim +1.7$), nearly all S is dissolved as S^{6+} (yellow). Here $w^m_{ST} \cong w^m_{S6+}$, and w^m_{ST} is instead controlled by equation (5c), which gives w^m_{S6+} as a simple function of f_{O2} and f_{S2}. At intermediate f_{O2} ($+0.7 \lesssim \Delta FMQ \lesssim +1.7$), the silicate melt transitions from being dominated by S^{2-} to S^{6+} (green). This region is narrow because the S speciation in the silicate melt is defined by equation (6c), which depends on $(f_{O2})^2$ (i.e., the difference in $\log_{10}[f_{O2}]$ between $[S^{6+}/S_T]^m$ = 0.1 and 0.9 is $\log_{10}[9] \sim 0.95$). The silicate melt

isopleths (the black dashed curves defining the edges of the green region) are sub-vertical (i.e., not precisely vertical) due to the P-dependence of f_{O2} on the FMQ buffer. When the value of Y is large, P is large, which leads to p_i deviating from f_i, causing the silicate melt isopleths to deviate from vertical (i.e., to curve to lower f_{O2}). They would, however, be vertical if plotted against $\log_{10}[f_{O2}]$ without normalisation to a buffer, given that C_{S2-} and C_{S6+} are assumed to be P-independent.

Unlike the speciation of S dissolved in the silicate melt, which depends only on f_{O2} via equation (6c), vapour speciation (i.e., x^v_{SO2}) depends on f_{S2} in addition to f_{O2} from equations (3b) and (8). Therefore, the boundaries separating where the vapour phase is dominated by S_2 (purple), both S_2+SO_2 (blue), and SO_2 (turquoise-green-yellow) depend on f_{O2} (see the vapour isopleths in Figure 3–Figure 5). However, the slopes of the boundaries depend on the choice of the Y variable and its value, as well as the silicate melt speciation (e.g., see the change in slope of $x^v_{SO2} = 0.9$ in Figure 4 where it enters the green region with increasing f_{O2}). The change in vapour speciation from dominantly S_2 to SO_2 occurs over a wider range of f_{O2} than the silicate melt speciation (compare the widths of the blue and green bands in silm, silicate melt; v, vapour; sulf^m, sulfide melt; anh, anhydrite; P^v_{sat}, pressure of vapour-saturation; f_{O2}, oxygen fugacity; w^m_{ST}, total dissolved S content of the silicate melt.

Figure 2 and

Figure 3–

Figure 5d) because f_{SO2} (and x^v_{SO2} via equation (8)) depends on $(f_{O2})^1$ from equation (3b), in contrast to $[S^{6+}/S^{2-}]^m$, which depends on $(f_{O2})^2$ from equation (6c).

Combining changes in silicate melt and vapour speciation, there are three main regions plus three transitional regions in $\log_{10}[f_{O2}]$-$\log_{10}[Y]$ space (Figure 3–Figure 5): at low f_{O2} and high Y, the vapour is S_2-dominated and the silicate melt is S^{2-}-dominated (purple); at higher f_{O2} and lower Y, the vapour contains both S_2 and SO_2 in similar concentrations, whereas the silicate melt is still S^{2-}-dominated (blue); at higher f_{O2} and lower Y, the vapour is now SO_2-dominated and the silicate melt is still S^{2-}-dominated (turquoise); at higher f_{O2} and most Y values shown, the vapour remains SO_2-dominated but the silicate melt contains both S^{2-} and S^{6+} in similar concentrations (green); at high f_{O2} and all Y values shown, the vapour is still SO_2-dominated but the silicate melt is S^{6+}-dominated (yellow); and there is also a small region where the vapour contains both S_2 and SO_2, and the silicate melt both S^{2-} and S^{6+}, in similar concentrations (light-turquoise region labelled $[S^{2-}+S^{6+}]^m+[S_2+SO_2]^v$ in Figure 3–Figure 5: it is not intersected in silm, silicate melt; v, vapour; sulf^m, sulfide melt; anh, anhydrite; P^v_{sat}, pressure of vapour-saturation; f_{O2}, oxygen fugacity; w^m_{ST}, total dissolved S content of the silicate melt.

Figure 2). At higher Y values than shown in Figure 3–Figure 5, there are three additional regions: at intermediate f_{O2}, the vapour is S_2-dominated and the silicate melt contains both S^{2-} and S^{6+} in similar concentrations; at high f_{O2} but intermediate Y, the vapour contains S_2 and SO_2 in similar concentrations and the silicate melt is S^{6+}-dominated; and at higher Y, the vapour is S_2-dominated and the silicate melt is still S^{6+}-dominated (a sketch of this topology is shown in the Supplementary Material).

Regions with a single dominant species in the silicate melt and vapour

For all three of our choices of a constant independent Y variable, curves (silm, silicate melt; v, vapour; sulf^{m}, sulfide melt; anh, anhydrite; P^{v}_{sat}, pressure of vapour-saturation; f_{O2}, oxygen fugacity; w^{m}_{ST}, total dissolved S content of the silicate melt.
Figure 2) and contours (Figure 3–Figure 5) of the dependent variables (Z) shown in the figures have constant slopes when there is a single dominant species in the silicate melt *and* a single dominant species in the vapour. For example, when the silicate melt is S^{2-}-dominated (purple-blue-turquoise),

$$w^{m}_{ST} \cong w^{m}_{S2-}, \tag{14a}$$

and when S^{6+}-dominated (yellow):

$$w^{m}_{ST} \cong w^{m}_{S6+}. \tag{14b}$$

Similarly, when the vapour is S_2-dominated (purple),

$$P \cong p_{S2} \cong f_{S2}, \tag{15a}$$

and when SO_2-dominated (turquoise-green-yellow):

$$P \cong p_{SO2} \cong f_{SO2}. \tag{15b}$$

When T is constant and there is only one dominant species in the silicate melt and one dominant species in the vapour

$$Z \propto (f_{O2})^{a}(Y)^{b}, \tag{16}$$

for all choices of Z and Y given here (see Table 1). Therefore, contours of constant Z in $\log_{10}(Y)$-$\log_{10}(f_{O2})$ plots have slopes (σ) ~ $-a/b$ (Figure 3–Figure 5) and, when Y is constant, curves of different Z have slopes (ς) ~ a (silm, silicate melt; v, vapour; sulf^{m}, sulfide melt; anh, anhydrite; P^{v}_{sat}, pressure of vapour-saturation; f_{O2}, oxygen fugacity; w^{m}_{ST}, total dissolved S content of the silicate melt.

Figure 2). Hence, the values of the slopes of the curves and contours of Z depend on the specific choice of the Y variable. Note that ς and σ are approximately, rather than exactly, equal to these values because: (1) the x-axis is $\log_{10}(f_{O2})$ relative to FMQ rather than strictly $\log_{10}(f_{O2})$; (2) partial pressure rather than fugacity is sometimes plotted, which are related through equation (8); and (3) although one species is dominant, the concentrations of the other species are not zero. At constant T, the relationships between f_{O2}, Y (f_{S2}, w^{m}_{ST}, and P), and Z (f_{S2}, f_{SO2}, P, w^{m}_{S2-}, w^{m}_{S6+}, and w^{m}_{ST}) when the silicate melt is S^{2-}-dominated and the vapour is S_2-dominated (purple), the silicate melt is S^{2-}-dominated but the vapour is SO_2-dominated (turquoise), and the silicate melt is S^{6+}-dominated and the vapour is SO_2-dominated (yellow) can be derived by variously substituting equations (14) and (15) into equations (3)–(8) and rearranging into the form of equation (16). These relationships are derived in the Supplementary Material; summarised (including ς and σ values) in Table 1; and labelled in silm, silicate melt; v, vapour; sulf^{m}, sulfide melt; anh, anhydrite;

P^{v}_{sat}, pressure of vapour-saturation; f_{O2}, oxygen fugacity; w^{m}_{ST}, total dissolved S content of the silicate melt.

Figure 2–Figure 5.

Regions with mixed speciation in the silicate melt or vapour

Changes in the slopes of curves (ς, silm, silicate melt; v, vapour; $sulf^{m}$, sulfide melt; anh, anhydrite; P^{v}_{sat}, pressure of vapour-saturation; f_{O2}, oxygen fugacity; w^{m}_{ST}, total dissolved S content of the silicate melt.
Figure 2) and contours (σ, Figure 3–Figure 5) occur for dependent variables (Z) when their slopes in $\log_{10}(Y)$-$\log_{10}(f_{O2})$ space differ in regions dominated by different species (i.e., S_2 (purple) vs. SO_2 (turquoise) in the vapour and/or S^{2-} (turquoise) vs. S^{6+} (yellow) in the silicate melt). The regions in which the slopes transition from one essentially constant value to another are where there is mixed speciation in the vapour (i.e., both S_2 and SO_2 in similar concentrations: blue) or in the silicate melt (i.e., both S^{2-} and S^{6+} in similar concentrations: green).

If the log-log slope of a Z variable with respect to f_{O2} has the same sign in the low- and high-f_{O2} regions on either side of one of the mixed species regions, the slope simply gets steeper or shallower along a constant Y path (silm, silicate melt; v, vapour; $sulf^{m}$, sulfide melt; anh, anhydrite; P^{v}_{sat}, pressure of vapour-saturation; f_{O2}, oxygen fugacity; w^{m}_{ST}, total dissolved S content of the silicate melt.

Figure 2–Figure 5). For example, with increasing f_{O2} and Y = constant w^{m}_{ST} = 400 ppm, the slope in silm, silicate melt; v, vapour; $sulf^{m}$, sulfide melt; anh, anhydrite; P^{v}_{sat}, pressure of vapour-saturation; f_{O2}, oxygen fugacity; w^{m}_{ST}, total dissolved S content of the silicate melt.

Figure 2d of $\log_{10}(P)$ vs. $\log_{10}(f_{O2})$ is $\varsigma \cong +1.0$ where the silicate melt is S^{2-}-dominated and the vapour is S_2-dominated (in the purple region). This is less than the value of $\varsigma \cong +1.5$ where the vapour is SO_2-dominated (in the turquoise region), but both slopes are positive (Table 1). For the contour plot in Figure 4c, this is shown as σ decreasing from -0.5 to -1.5, but both being negative. This is because when the silicate melt is S^{2-}-dominated, the log-log slope for $Z = p_{SO2}$ is steeper than for $Z = p_{S2}$ ($\varsigma \cong +1.5$ vs. +1.0 or $\sigma \cong -1.5$ vs. -0.5 in the purple-blue-turquoise regions in silm, silicate melt; v, vapour; $sulf^{m}$, sulfide melt; anh, anhydrite; P^{v}_{sat}, pressure of vapour-saturation; f_{O2}, oxygen fugacity; w^{m}_{ST}, total dissolved S content of the silicate melt.

Figure 2d and Figure 4a–c). Therefore, the curves cross when $p_{S2} = p_{SO2}$ (at the point labelled β in the blue region of silm, silicate melt; v, vapour; $sulf^{m}$, sulfide melt; anh, anhydrite; P^{v}_{sat}, pressure of vapour-saturation; f_{O2}, oxygen fugacity; w^{m}_{ST}, total dissolved S content of the silicate melt.

Figure 2d). Hence, along this path P is essentially equal to p_{S2} when S_2 dominates the vapour ($\varsigma \cong +1.0$ or $\sigma \cong -0.5$, purple), steepens continuously in the region where the concentration of SO_2 in the vapour increases (blue), and is then well approximated by p_{SO2} when SO_2 dominates the vapour ($\varsigma \cong +1.5$ or $\sigma \cong -1.5$, turquoise).

If the log-log slope of a Z variable with respect to f_{O2} has opposite signs on the two sides of a mixed speciation region, a maximum (positive to negative slope with increasing f_{O2}) or minimum

(negative to positive slope with increasing f_{O2}) in Z occurs (silm, silicate melt; v, vapour; sulf^m, sulfide melt; anh, anhydrite; P^v_{sat}, pressure of vapour-saturation; f_{O2}, oxygen fugacity; w^m_{ST}, total dissolved S content of the silicate melt.

Figure 2–Figure 5). For example, for Y = constant f_{S2}, there is a minimum in $Z = w^m_{ST}$ at $[S^{6+}/S_T]^m = 0.5$ (this corresponds to a maximum in $Z = \log_{10}[w^m_{ST}]$ contours), where the silicate melt changes from being S^{2-}- to S^{6+}-dominated (i.e., the green region in silm, silicate melt; v, vapour; sulf^m, sulfide melt; anh, anhydrite; P^v_{sat}, pressure of vapour-saturation; f_{O2}, oxygen fugacity; w^m_{ST}, total dissolved S content of the silicate melt.

Figure 2a and

Figure 3c). This is an example of an SS^{min} on a specific path of increasing f_{O2} (i.e., f_{S2} and T are constant). However, there are paths with monotonically increasing f_{O2} and variable f_{S2} for which a minimum is not encountered (e.g., all linear paths on Figure 3c with $\sigma \geq +1$ or $\sigma \leq -3$). There is also an SS^{min} when Y = constant P, as shown by the white S_T curve in silm, silicate melt; v, vapour; sulf^m, sulfide melt; anh, anhydrite; P^v_{sat}, pressure of vapour-saturation; f_{O2}, oxygen fugacity; w^m_{ST}, total dissolved S content of the silicate melt.

Figure 2e and by the maxima in the $\log_{10}[w^m_{ST}]$ contours in
Figure 5c. As for the constant f_{S2}-path, this minimum also occurs at $[S^{6+}/S_T]^m = 0.5$ (i.e., in the green region). Similarly, there are paths with monotonically increasing f_{O2} and variable P that do not encounter the minimum (e.g., all $\log_{10}(f_{O2})$-$\log_{10}(P)$ paths on
Figure 5c with $\sigma \geq +1.5$ and $\sigma \leq -0.5$).

These SS^{min} occur because curves and contours of w^m_{ST} have opposite slopes at lower-f_{O2} where S^{2-} dominates the silicate melt compared to at higher-f_{O2} where S^{6+} dominates (silm, silicate melt; v, vapour; sulf^m, sulfide melt; anh, anhydrite; P^v_{sat}, pressure of vapour-saturation; f_{O2}, oxygen fugacity; w^m_{ST}, total dissolved S content of the silicate melt.

Figure 2a and e,

Figure 3c, and
Figure 5c). This occurs because O_2 in the vapour is on the product side of reaction (4a) when sulfur dissolves dominantly as S^{2-} in the silicate melt, but on the reactant side when sulfur dissolves dominantly as S^{6+} in the silicate melt in reaction (5a). This is true whether the reactions are written for dissolving SO_2 or S_2 from the vapour into the silicate melt. Thus, for any path of constant f_{S2} or P (i.e., horizontal slices in Figure 3c or
Figure 5c, respectively), w^m_{ST} reaches a minimum at $[S^{6+}/S_T]^m = 0.5$.

When $Y = w^m_{ST}$ and is held constant as f_{O2} increases, the SS^{min} manifests itself as a *maximum* in $Z = P$ in silm, silicate melt; v, vapour; sulf^m, sulfide melt; anh, anhydrite; P^v_{sat}, pressure of vapour-saturation; f_{O2}, oxygen fugacity; w^m_{ST}, total dissolved S content of the silicate melt.

Figure 2d (and corresponding minima in $Z = P$ contours in the green region in Figure 4c). This is because at the SS^{min}, a higher P is required to maintain the same S content in the vapour-saturated silicate melt. Since SO_2 is the dominant vapour species on both sides of the maximum in P (i.e., $P \cong p_{SO2}$), there is also a maximum in p_{SO2} at essentially the same point (and corresponding minima in $Z = f_{SO2}$ contours in Figure 4b). The change in sign of the slope of p_{SO2} at the maximum with increasing f_{O2} (e.g., from $\varsigma \sim +1.5$ to -0.5 in silm, silicate melt; v, vapour; sulf^m, sulfide melt; anh,

anhydrite; P^{v}_{sat}, pressure of vapour-saturation; f_{O2}, oxygen fugacity; w^{m}_{ST}, total dissolved S content of the silicate melt.

Figure 2d) is due to the crossover of S^{2-} to S^{6+} as the dominant species in the silicate melt (see "Regions with a single dominant species in the silicate melt and vapour"). Note that $Z = p_{S2}$ also has a maximum in silm, silicate melt; v, vapour; sulf^{m}, sulfide melt; anh, anhydrite; P^{v}_{sat}, pressure of vapour-saturation; f_{O2}, oxygen fugacity; w^{m}_{ST}, total dissolved S content of the silicate melt.

Figure 2d (and corresponding minima in $Z = f_{S2}$ contours in Figure 4a) with increasing f_{O2} in the same vicinity as the maxima in P and p_{SO2}. This is also because of the change in silicate melt speciation: however, since $p_{S2} \ll p_{SO2}$, the maximum in p_{S2} has negligible influence on the maximum in P.

The maxima (and corresponding minima in the equivalent contours) in p_{SO2}, p_{S2}, and P all occur where the silicate melt speciation is mixed. The maxima in p_{SO2} and P essentially coincide because $P \cong p_{SO2}$, but the p_{S2} maximum is at a different f_{O2}, and none (unlike the w^{m}_{ST} minima) occur exactly at $[S^{6+}/S_T]^{m} = 0.5$ (e.g., compare silm, silicate melt; v, vapour; sulf^{m}, sulfide melt; anh, anhydrite; P^{v}_{sat}, pressure of vapour-saturation; f_{O2}, oxygen fugacity; w^{m}_{ST}, total dissolved S content of the silicate melt.

Figure 2c and d). When the silicate melt has mixed speciation, equation (2) is needed rather than the approximations of equations (14a) and (14b). Substituting equations (4c) and (5c) into equation (2), and converting to partial pressure using equation (8) gives:

$$f_{S2} = \gamma_{S2} p_{S2} = (w^{m}_{ST}/(C_{S2-}(f_{O2})^{-0.5} + C_{S6+}(f_{O2})^{1.5}))^2, \quad (17a)$$

and substituting equation (3b) gives:

$$f_{SO2} = \gamma_{SO2} p_{SO2} = K_3 w^{m}_{ST}/((C_{S2-}(f_{O2})^{0.5} + C_{S6+}(f_{O2})^{2.5})). \quad (17b)$$

The f_{O2} values at the maximum for p_{S2} and p_{SO2} are given by differentiating equations (17a) and (17b) with respect to f_{O2} and solving for f_{O2} when this equals zero. As the relationships between p_{S2} and p_{SO2} with f_{O2} are different, the f_{O2} values of the maxima are also different.

We refer to the f_{O2} where the w^{m}_{ST} minimum or P maximum occurs as the ${}^{SSmin}f_{O2}$, but it can *only* be defined for silicate melt + vapour at a given T and for a choice of $Y = f_{S2}$, w^{m}_{ST}, or P. The SS^{min} always occurs when both S^{2-} and S^{6+} are dissolved in the silicate melt in similar concentrations, although it only occurs at $[S^{6+}/S_T]^{m} = 0.5$ when $Y = f_{S2}$ or w^{m}_{ST}. Moreover, the minimum is not symmetric with changing f_{O2} (see silm, silicate melt; v, vapour; sulf^{m}, sulfide melt; anh, anhydrite; P^{v}_{sat}, pressure of vapour-saturation; f_{O2}, oxygen fugacity; w^{m}_{ST}, total dissolved S content of the silicate melt.

Figure 2a, d, and e; and

Figure 3–

Figure 5c) because the stoichiometry of the reactions for sulfur dissolution as S^{2-} and S^{6+} differ. The different manifestations of the SS^{min} are related but not identical, reflecting the different f_{S2}–

f_{O2} paths for different choices of Y. For example, there is a P maximum when $Y = w^m_{ST}$ (silm, silicate melt; v, vapour; $sulf^m$, sulfide melt; anh, anhydrite; P^v_{sat}, pressure of vapour-saturation; f_{O2}, oxygen fugacity; w^m_{ST}, total dissolved S content of the silicate melt.

Figure 2d and Figure 4c), but no P maximum when $Y = f_{S2}$ (silm, silicate melt; v, vapour; $sulf^m$, sulfide melt; anh, anhydrite; P^v_{sat}, pressure of vapour-saturation; f_{O2}, oxygen fugacity; w^m_{ST}, total dissolved S content of the silicate melt.

Figure 2b and

Figure 3b) or P (silm, silicate melt; v, vapour; $sulf^m$, sulfide melt; anh, anhydrite; P^v_{sat}, pressure of vapour-saturation; f_{O2}, oxygen fugacity; w^m_{ST}, total dissolved S content of the silicate melt.

Figure 2f, by definition). Similarly, there is a w^m_{ST} minimum when $Y = f_{S2}$ (silm, silicate melt; v, vapour; $sulf^m$, sulfide melt; anh, anhydrite; P^v_{sat}, pressure of vapour-saturation; f_{O2}, oxygen fugacity; w^m_{ST}, total dissolved S content of the silicate melt.

Figure 2a and

Figure 3c) and P (silm, silicate melt; v, vapour; $sulf^m$, sulfide melt; anh, anhydrite; P^v_{sat}, pressure of vapour-saturation; f_{O2}, oxygen fugacity; w^m_{ST}, total dissolved S content of the silicate melt.

Figure 2e and

Figure 5c), but not when $Y = w^m_{ST}$ (silm, silicate melt; v, vapour; $sulf^m$, sulfide melt; anh, anhydrite; P^v_{sat}, pressure of vapour-saturation; f_{O2}, oxygen fugacity; w^m_{ST}, total dissolved S content of the silicate melt.

Figure 2c, again by definition). This highlights the importance of the choice of the third independent variable for silicate melt + vapour in understanding the occurrence of the SS^{min}, which is required to specify the path followed by the system with changing f_{O2}.

<u>Silicate melt + vapour + (sulfide melt and/or anhydrite)</u>

For Y values below the curves indicating sulfide melt-saturation (the grey solid curves labelled "$sulf^m$") or anhydrite-saturation (the grey dashed curves labelled "*anh*") in Figure 3–Figure 5 (and shown as vertical grey lines in silm, silicate melt; v, vapour; $sulf^m$, sulfide melt; anh, anhydrite; P^v_{sat}, pressure of vapour-saturation; f_{O2}, oxygen fugacity; w^m_{ST}, total dissolved S content of the silicate melt.

Figure 2), the two-phase silicate melt + vapour assemblage is stable. At Y values above these curves, the silicate melt is vapour-undersaturated but instead saturated with sulfide melt and/or

anhydrite, which will be discussed in "Silicate melt + (vapour and/or sulfide melt and/or anhydrite)". Therefore, the calculations involving silicate melt + vapour in this region describe metastable equilibria.

This section describes the behaviour on the grey curves in Figure 3–Figure 5, where silicate melt + vapour in the model ternary system are stable and saturated with sulfide melt and/or anhydrite. In our model ternary system, there are still only two phases (silicate melt + vapour) and therefore $F = 3$. Hence, given T and f_{O2}, the curve for sulfide melt-saturation is defined by a particular value of $Y = \mu^m_{FeS}$ that is equal to that of FeS in the saturating sulfide melt. In practice we apply the formulation of O'Neill (2020) to calculate S^{2-}CSS for the silicate melt, which is conceptually equivalent to holding μ^m_{FeS} equal to a constant chemical potential of sulfide melt at the relevant conditions. In our calculations, we assume the sulfide melt is pure FeS (i.e., $\mu_{FeS} = \mu_{FeS}°$), although this could be modified. Similarly, the curve for anhydrite-saturation is defined by $Y = \mu^m_{CaSO4}$. Again, although S^{6+}CAS is calculated based on Chowdhury and Dasgupta (2019), this is conceptually equivalent to holding μ^m_{CaSO4} equal to a constant chemical potential of pure anhydrite at the relevant conditions. The stable saturation condition (i.e., sulfide melt- or anhydrite-saturation) is the one with the lowest w^m_{ST}.

If the silicate melt + vapour assemblage is saturated with either sulfide melt or anhydrite, P and w^m_{ST} are no longer independent variables. Therefore, having chosen values of T, f_{O2}, and μ^m_{FeS} or μ^m_{CaSO4} (which confines the state of the system to the $sulf^m$ or *anh* curves), both P and w^m_{ST} are fixed, as can be visualized in Figure 4–Figure 5c. Moreover, when the silicate melt + vapour assemblage is saturated with both sulfide melt and anhydrite at a fixed T, three independent variables are specified, so no other parameters can be chosen independently. This is demonstrated graphically in Figure 4–Figure 5c by the grey star, which for a given T has fixed values of P, f_{O2}, and w^m_{ST} at the unique intersection of the grey solid and dashed curves. We can thus describe quantitatively with our model a constant-T, increasing-f_{O2} path for an assemblage containing silicate melt + vapour + (sulfide melt and/or anhydrite). The variations in the values of the Z variables along this path can be read from the contours crossed by the grey curves in Figure 3–Figure 5 and Figure 6a and b show the variation in w^m_{ST} and P on this path.

At low f_{O2} (ΔFMQ $\lesssim$ +0.6), the independent variables are T, f_{O2}, and μ_{FeS}: the silicate melt is S^{2-}-dominated and saturated with vapour and sulfide melt (i.e., the solid grey $sulf^m$ curves in the purple-blue-turquoise regions of Figure 3–Figure 5 and 6a–b). Therefore, w^m_{ST} is controlled by S^{2-} CSS from equations (14a) and (9), hence:

$$w^m_{ST} \cong w^m_{S2-} = w^m_{S2\text{-}CSS}. \quad (18)$$

S^{2-}CSS is sub-parallel to the $\log_{10}[w^m_{ST}] \sim 3$ contour, although there is a small increase in $w^m_{S2\text{-}CSS}$ with increasing f_{O2} because: (1) there is always some S present in the silicate melt as S^{6+}; and (2) $w^m_{S2\text{-}CSS}$ depends on P and $[Fe^{3+}/Fe_T]^m$ (O'Neill 2020), both of which increase with increasing f_{O2}. Nevertheless, w^m_{ST} is nearly constant and therefore for all practical purposes P (and the p_i's) behave as for the case when T-f_{O2}-w^m_{ST} were independent variables (silm, silicate melt; v, vapour; $sulf^m$, sulfide melt; anh, anhydrite; P^v_{sat}, pressure of vapour-saturation; f_{O2}, oxygen fugacity; w^m_{ST}, total dissolved S content of the silicate melt.

Figure 2c–d and Figure 4).

At intermediate f_{O2} ($+0.6 \lesssim \Delta FMQ < +1.5$), the conditions remain the same ($Y = \mu_{FeS}$; the silicate melt is saturated with vapour and sulfide melt, and $w^m_{S2-} = w^m_{S2\text{-}CSS}$), but the silicate melt contains significant quantities of both S^{2-} and S^{2+} (i.e., the solid grey curves in the green region of Figure 3– Figure 5 and Figure 6a–b). As the solubility of S^{6+} increases, w^m_{ST} increases based on equation (10) (e.g., in Figure 4c where the nearly horizontal grey $sulf^m$ curve turns steeply upward as it enters the green region with increasing f_{O2}). With increasing f_{O2}, w^m_{ST} increases until the silicate melt reaches anhydrite-saturation when $w^m_{S6+} = w^m_{S6+CAS}$ from equation (11). At this point, the silicate melt is saturated with vapour + sulfide melt + anhydrite, and the independent variables are T, μ_{FeS}, and μ_{CaSO4}. It is important to emphasize that for this choice of independent variables, at a given T, the vapour-saturated silicate melt defines a unique point in Figure 3 and Figure 5 (the grey star at the intersection of the solid and dashed grey curves) and fixes the values of all other intensive parameters. Therefore, combining equations (2), (9), and (11):

$$w^m_{ST} = w^m_{S2\text{-}CSS} + w^m_{S6+CAS}, \tag{19a}$$

and substituting equations (9) and (11) into (6c):

$$w^m_{S6+CAS}/w^m_{S2\text{-}CSS} = [C_{S6+}/C_{S2-}](f_{O2})^2. \tag{19b}$$

This corresponds to the maximum w^m_{ST} at $\Delta FMQ \cong +1.5$ (i.e., the star on the grey curves in Figure 3c, Figure 5c, and Figure 6a: this multiply saturated point is not shown in Figure 4 because it occurs above the w^m_{ST} range of the figure).

At higher f_{O2} levels than those described in the previous paragraph (i.e., $\Delta FMQ > +1.5$), the vapour-saturated silicate melt is no longer saturated with sulfide melt. However, it is still saturated with anhydrite (independent variables = T, f_{O2}, and μ_{CaSO4}) and thus follows the dashed grey *anh* curves. The silicate melt is S^{6+}-dominated and w^m_{S6+} is fixed at S^{6+}CAS (which is taken to be a constant); hence, w^m_{S2-} is given by equation (6c) rather than S^{2-}CSS. Therefore, the amount of S^{2-} in the silicate melt decreases whilst w^m_{S6+} remains constant. Hence, w^m_{ST} initially decreases with increasing f_{O2} based on equation (12), resulting in the maximum at the star (this is most visible in Figure 6a). At sufficiently high f_{O2} ($\Delta FMQ > +2.0$), w^m_{ST} is essentially constant at S^{6+}CAS from equations (14b) and (11)

$$w^m_{ST} \cong w^m_{S6+} = w^m_{S6+CAS}, \tag{20}$$

and independent of P and f_{O2} given the parameterisation we have used. Hence, w^m_{S6+CAS} is essentially parallel to the $\log_{10}[w^m_{ST}] \approx 4$ contour over most of the yellow regions in Figure 3c and Figure 5c, except for a small (but effectively undetectable) deviation because some S^{2-} is always present, which decreases with increasing f_{O2}.

At low f_{O2} when f_{O2} is increased, w^m_{S6+} increases while w^m_{S2-} is essentially constant at $w^m_{S2\text{-}CSS}$. Conversely, at high f_{O2} when f_{O2} is decreased, w^m_{ST} increases because w^m_{S2-} increases while w^m_{S6+} is constant at w^m_{S6+CAS}. Thus, there is a maximum in w^m_{ST} when the silicate melt is saturated with vapour + sulfide melt + anhydrite (i.e., the star in

Figure 3c,

Figure 5c, and 6a). Whilst the system is at this particular T-P-f_{O2} value, w^m_{ST} is fixed and any excess sulfur in the system above this value would form more vapour, sulfide melt, and/or anhydrite: hence, it is a *global* SS^{max}. A maximum in P also occurs at this f_{O2} (

Figure 6b) because a higher P is required to keep the total S content dissolved in the silicate melt as described in "Regions with mixed speciation in the silicate melt or vapour". Although this maximum occurs in the vicinity of the SS^{min} (described in "Regions with mixed speciation in the silicate melt or vapour"), it follows a different path that results in an SS^{max}.

<u>Silicate melt + (vapour and/or sulfide melt and/or anhydrite)</u>

For Y values above the grey curves in

Figure 3–

Figure 5, the stable phase assemblage is no longer silicate melt + vapour. The contours for vapour-saturated silicate melt shown beyond these curves are metastable in these regions. Since in our treatment the silicate melt is confined to the model ternary system and it is vapour-undersaturated, the silicate melt is the only stable phase. Therefore, $\varphi = 1$ and $F = 4$, meaning four independent variables are needed to specify the state of the system. Although silicate melt is the only stable phase in the model ternary system under these conditions, the silicate melt can be saturated with sulfide melt and/or anhydrite (which are not in the ternary system) if the values of μ_{FeS} and/or μ_{CaSO4} in the silicate melt correspond to the values of these phases. In this section, we choose T, f_{O2}, P and either μ_{FeS} if the silicate melt is sulfide melt-saturated or μ_{CaSO4} if it is anhydrite-saturated. If the silicate melt is both sulfide melt- and anhydrite-saturated, only two of the three other variables (T, f_{O2}, and P) can be independent. For given values of T, f_{O2}, and P (and parameterizations of S^{2-}CSS, S^{6+}CAS, C_{S2-}, and C_{S6+}), w^m_{ST} at sulfide melt-saturation can be calculated using equation (10) and at anhydrite-saturation using equation (12). As before, the stable saturation condition (i.e., sulfide melt- or anhydrite-saturation) is the one with the lowest w^m_{ST}.

Figure 5f shows in P-f_{O2} space (at T = 1200°C) the phase(s) with which the silicate melt on the model ternary plane is saturated: the dark and light grey regions are for sulfide melt- and anhydrite-saturation, respectively, and the coloured regions are for vapour-saturation as described in "Silicate melt + vapour". Where these regions intersect, the silicate melt is saturated with two of the three other phases and these curves define fully constrained paths in P-f_{O2} space at constant T. The behaviour of w^m_{ST} and P with increasing f_{O2} for silicate melt saturated with vapour + sulfide melt or vapour + anhydrite are described in "Silicate melt + vapour + (sulfide melt and/or anhydrite)". With increasing P, for silicate melt saturated with sulfide melt + anhydrite (without vapour), w^m_{ST}

decreases and f_{O2} is almost constant. The three curves (silicate melt + vapour + sulfide melt; silicate melt + vapour + anhydrite; and silicate melt + sulfide melt + anhydrite) meet at a point (the star), where silicate melt is saturated with vapour, sulfide melt, and anhydrite), corresponding to a global maximum in w^m_{ST} for a given T (described in "Silicate melt + vapour + (sulfide melt and/or anhydrite)").

We now explore how w^m_{ST} changes along isobaric paths of increasing f_{O2}, where P is above or below P = 1543 bar where silicate melt is multiply-saturated with vapour, sulfide melt, and anhydrite (i.e., the grey star in Figure 5g and Figure 6c and e). At P > 1543 bar, the silicate melt is vapour-undersaturated but the trend of w^m_{ST} with increasing f_{O2} is similar to the case where vapour-saturation occurs in addition to sulfide melt- and/or anhydrite-saturation as described in "Silicate melt + vapour + (sulfide melt and/or anhydrite)" (e.g., compare Figure 6a and c). The maximum without vapour but sulfide melt + anhydrite saturation is lower than with vapour + sulfide melt + anhydrite, as the latter is a global maximum at a fixed T. The maximum S content at a given P occurs at a unique f_{O2} (depending on the composition of the silicate component) at the near vertical curve defining saturation of the silicate melt with both sulfide melt and anhydrite. Both μ_{FeS} and μ_{CaSO4} are specified in addition to P at this point, and therefore f_{O2} is fixed for this set of three independent variables (in addition to T).

At P < 1543 bar, the stable isobaric path crosses into the stable vapour-saturated field at intermediate f_{O2} (e.g., at the grey solid curve in Figure 5g, described in "Silicate melt + vapour + (sulfide melt and/or anhydrite)"). The behaviour (and calculations – equation (10)) at low f_{O2} (ΔFMQ $\lesssim$ +0.8), when the silicate melt is only saturated with sulfide melt, is the same as at higher P (i.e., compare the black solid curves in Figure 6c and e: these two curves are nearly identical since the dependence of w^m_{S2-CSS} on P is minor; O'Neill, 2020). A local maximum (ΔFMQ $\cong$ +0.8) occurs when the silicate melt is saturated with both sulfide melt and vapour (i.e., labelled "δ" at the solid grey vertical line in

Figure 6e). When f_{O2} is further increased beyond this point (+0.8 $\lesssim$ ΔFMQ $\lesssim$ +3.6), the silicate melt is only vapour-saturated, and w^m_{ST} displays the SS^{min} as described in "Regions with mixed speciation in the silicate melt or vapour" (i.e., labelled "ε" on the dotted black curve in

Figure 6e). When $w^m_{S6+} = w^m_{S6+CAS}$ (ΔFMQ $\cong$ +3.6), the silicate melt is saturated with vapour and anhydrite (e.g., the grey dashed vertical line in

Figure 6e). There is a small maximum at (anhydrite + vapour)-saturation (labelled "ζ"), but it cannot be distinguished in

Figure 6e because for the isobar chosen it is at sufficiently high f_{O2} that there is essentially only S^{6+} (i.e., very little S^{2-}) dissolved in the silicate melt at this point. Therefore, although w^m_{S2-} decreases with increasing f_{O2} beyond this point, it is already so low that the magnitude of the decrease in w^m_{ST} is insignificant. At f_{O2} values above this point (ΔFMQ $\gtrsim$ +3.6), the silicate melt is only saturated with anhydrite (i.e., the dashed black curve in

Figure 6e) and behaves as described previously under these conditions. For a given P, along all isobaric paths of increasing f_{O2} when vapour-saturation is encountered (i.e., P < 1543 bars), there is an SS^{max} when the silicate melt is saturated with sulfide melt + vapour (δ, which gets larger with increasing P); an SS^{min} when the silicate melt is only vapour-saturated (ε); and another SS^{max} when the silicate melt is saturated with anhydrite + vapour (ζ).

Isothermal, decompression-induced degassing

The examples developed in "Independent variables of T, f_{O2}, f_{S2}, w^m_{ST}, P, μ_{FeS}, and μ_{CaSO4}" and silm, silicate melt; v, vapour; sulf^m, sulfide melt; anh, anhydrite; P^v_{sat}, pressure of vapour-saturation; f_{O2}, oxygen fugacity; w^m_{ST}, total dissolved S content of the silicate melt.

Figure 2–Figure 5 do not apply to the f_{O2}–f_{S2} paths followed by magmas as they degas on decompression (or due to crystallisation) under equilibrium conditions because f_{O2} is not an independent variable in this process. We have evaluated whether the SS^{min} has any impact on closed- and open-system degassing during isothermal decompression using our simple model ternary system. Inclusion of other volatiles (e.g., H and C) would add complexity to the system and are important for getting the details correct for simulation of degassing in nature (e.g., Moretti *et al.* 2003; Moretti and Papale 2004; Burgisser and Scaillet 2007; Gaillard and Scaillet 2009, 2014; Wallace and Edmonds 2011; Gaillard *et al.* 2011, 2015; Burgisser *et al.* 2015; Iacovino 2015; Liggins *et al.* 2020). However, their exclusion here allows us to isolate the behaviour of sulfur during degassing.

We model closed-system degassing by decreasing P at constant T and constant bulk composition for the two-phase system silicate melt + vapour; hence, the independent variables are T, P, and bulk composition. A closed-system requires the bulk composition of the system (i.e., silicate melt ± vapour) to be constant at all P. The bulk composition comprises the proportions of the silicate melt component, total S_2, and O_2 (the latter is the O_2 in excess of that in the model silicate component). For open-system degassing, any vapour present at each P step (1 bar increments) is removed from the system. Hence, the bulk composition of the system changes during depressurisation and the silicate melt composition becomes the bulk composition of the system for the subsequent P step. We do not allow sulfide melt or anhydrite to be present; hence, in some regions the silicate melt + vapour assemblage encountered during degassing is metastable (to the left of the solid grey curve in Abbreviations: sil^m, silicate melt; v, vapour; sulf^m, sulfide melt; anh, anhydrite; MORB, mid-ocean ridge basalts; OIB, ocean island basalts; and Arc, arc basalts.
Figure 7a). Results of closed- and open-system degassing calculations are essentially indistinguishable (Figure 8), hence we only discuss closed-system degassing calculations.

For a particular bulk composition, when $P > P^v_{sat}$ (pressure of vapour-saturation; above the solid black curve in Abbreviations: sil^m, silicate melt; v, vapour; sulf^m, sulfide melt; anh, anhydrite; MORB, mid-ocean ridge basalts; OIB, ocean island basalts; and Arc, arc basalts.
Figure 7), the system is vapour-undersaturated and only silicate melt is present. At $P = P^v_{sat}$ (on the solid black curve), the system is still 100 % silicate melt, but the silicate melt is vapour-saturated (i.e., equation (7) is satisfied using equations (3b), (4c), (5c), (8), and the bulk composition of the system). When $P < P^v_{sat}$ (below the solid black curve), the silicate melt is supersaturated with respect to vapour, such that vapour exsolves from the silicate melt and the two phases coexist under equilibrium conditions. The 5000 ppm contour is the locus of P^v_{sat} (i.e., the P at which degassing begins; Abbreviations: sil^m, silicate melt; v, vapour; sulf^m, sulfide melt; anh, anhydrite; MORB, mid-ocean ridge basalts; OIB, ocean island basalts; and Arc, arc basalts.
Figure 7c) for a silicate melt corresponding to the bulk composition of the system, where the white diamond indicates $^{SSmin}f_{O2}$ (i.e., ΔFMQ+1.30 for these parameters, at the maximum of the black curve).

If the silicate melt starts off more reduced than $^{SSmin}f_{O2}$, f_{O2} *decreases* with decreasing P during closed-system degassing (e.g., the yellow curves in Abbreviations: sil^m, silicate melt; v, vapour; sulf^m, sulfide melt; anh, anhydrite; MORB, mid-ocean ridge basalts; OIB, ocean island basalts; and Arc, arc basalts.

Figure 7d and g, and 8b). This reflects that although the silicate melt is S^{2-}-dominated, the vapour is S_2-dominated and/or SO_2-dominated (Abbreviations: sil^m, silicate melt; v, vapour; sulf^m, sulfide melt; anh, anhydrite; MORB, mid-ocean ridge basalts; OIB, ocean island basalts; and Arc, arc basalts.

Figure 7f), so O_2 is consumed during degassing to convert S^{2-} dissolved in the silicate melt into the more oxidised S_2 and SO_2 vapour species (see reaction (4a) and the reaction generated by subtracting (3a) from (4a)). Therefore, reduction of the system (i.e., a decrease in f_{O2}) must occur for degassing under these conditions, although this effect is buffered by changes in $[Fe^{3+}/Fe_T]^m$, which are included in our calculations. However, if the silicate melt starts off more oxidised than $^{Ssmin}f_{O2}$, f_{O2} *increases* with decreasing P during closed-system degassing (e.g., the turquoise curve in Abbreviations: sil^m, silicate melt; v, vapour; sulf^m, sulfide melt; anh, anhydrite; MORB, mid-ocean ridge basalts; OIB, ocean island basalts; and Arc, arc basalts.

Figure 7d and g, and 8b). This reflects that the silicate melt is S^{6+}-dominated but the vapour is SO_2-dominated (Abbreviations: sil^m, silicate melt; v, vapour; sulf^m, sulfide melt; anh, anhydrite; MORB, mid-ocean ridge basalts; OIB, ocean island basalts; and Arc, arc basalts.

Figure 7f), so O_2 is generated during degassing to convert SO_4^{2-} dissolved in the silicate melt into the more reduced SO_2 vapour species (see the reaction generated by subtracting (3a) from (5a)). Hence, oxidation of the system (i.e., an increase in f_{O2}) must occur for degassing under these conditions. Close inspection of Abbreviations: sil^m, silicate melt; v, vapour; sulf^m, sulfide melt; anh, anhydrite; MORB, mid-ocean ridge basalts; OIB, ocean island basalts; and Arc, arc basalts.

Figure 7d demonstrates that for a narrow range of bulk compositions that start degassing close to, but slightly more reducing than, $^{SSmin}f_{O2}$, f_{O2} initially increases and then decreases at lower P. In contrast to bulk compositions that are displaced in f_{O2} from $^{SSmin}f_{O2}$ by more than ~0.1 log units, there is minimal change in f_{O2} during depressurisation for bulk compositions that start close to $^{SSmin}f_{O2}$ (e.g., the green curves in Abbreviations: sil^m, silicate melt; v, vapour; sulf^m, sulfide melt; anh, anhydrite; MORB, mid-ocean ridge basalts; OIB, ocean island basalts; and Arc, arc basalts.

Figure 7d and g, and 8b).

At constant bulk composition when $P < P^v_{sat}$, w^m_{ST} decreases monotonically with decreasing P to 1 bar (Abbreviations: sil^m, silicate melt; v, vapour; sulf^m, sulfide melt; anh, anhydrite; MORB, mid-ocean ridge basalts; OIB, ocean island basalts; and Arc, arc basalts.

Figure 7c and 8c). Hence, the SS^{min} is not encountered in our simple system during closed-system, depressurisation-induced degassing because changes in f_{O2} do not cause the silicate melt to cross the SS^{min}. However, the shapes of the w^m_{ST} with decreasing P are different at the SS^{min} (roughly linear) compared to either side (concave down). With decreasing P, f_{S2} (Abbreviations: sil^m, silicate melt; v, vapour; sulf^m, sulfide melt; anh, anhydrite; MORB, mid-ocean ridge basalts; OIB, ocean island basalts; and Arc, arc basalts.

Figure 7a and 8a) and f_{SO2} (Abbreviations: sil^m, silicate melt; v, vapour; sulf^m, sulfide melt; anh, anhydrite; MORB, mid-ocean ridge basalts; OIB, ocean island basalts; and Arc, arc basalts.

Figure 7b) always decrease; the rate of decrease depends on the bulk composition of the system. The rate of change is controlled by the trade-off between decreasing w^m_{ST} and decreasing or increasing f_{O2} to the left and right of SS^{min}, respectively, through equations (17a) and (17b).

Implications of SS^{min} and SS^{max} for magmatic and volcanic processes

The SS^{min} for silicate melt + vapour and the SS^{max} for silicate melt ± vapour + sulfide melt + anhydrite occur in a similar f_{O2} range since both features depend on the silicate melt having mixed S speciation ("Independent variables of T, f_{O2}, f_{S2}, w^m_{ST}, P, μ_{FeS}, and μ_{CaSO4}"). The SS^{min} manifests when T (held constant) and f_{O2} are independent variables, and f_{S2}, w^m_{ST}, or P are the third independent variable and held constant or varied in particular ways (see "Regions with mixed speciation in the silicate melt or vapour"; silm, silicate melt; v, vapour; $sulf^m$, sulfide melt; anh, anhydrite; P^v_{sat}, pressure of vapour-saturation; f_{O2}, oxygen fugacity; w^m_{ST}, total dissolved S content of the silicate melt.

Figure 2–Figure 5). The SS^{min} reflects the prominent "valleys" – centered where the silicate melt has mixed S speciation – in the isothermal surfaces showing w^m_{ST} as a function of f_{S2} or P vs. f_{O2} (

Figure 3c and
Figure 5c). An alternative expression of the SS^{min} is the prominent "ridge" in the topography of the isothermal P surface plotted as a function of w^m_{ST} vs. f_{O2} (Figure 4c). However, there are simple linear paths that cross the valley (or ridge) with increasing f_{O2} in

Figure 3–
Figure 5c for which there is no SS^{min}. There are also geological important paths (including closed- or open-system depressurisation; "Isothermal, decompression-induced degassing") that nearly parallel the valley floor (or ridge crest) and therefore do no encounter an SS^{min}.

Our model calculations place the SS^{min} for this Hawaiian basalt composition at 1200 °C at ${}^{SSmin}f_{O2} \cong \Delta FMQ+1.2$. For comparison, this is slightly more oxidised than Hawaiian basalts (ΔFMQ-0.5 to +1.0; Moussallam *et al.* 2016; Brounce *et al.* 2017; Lerner *et al.* 2021) and more oxidised than mid-ocean ridge basalts (MORB), but within the range measured in arc and ocean island basalts (OIB) (e.g., Cottrell et al., 2021). The position of ${}^{SSmin}f_{O2}$ will depend on T, composition of the silicate component, and additional volatile components (e.g., H_2O, CO_2). To explore how the effects described here vary with T and melt composition, a robust parameterisation of C_{S6+} is required to model S solubility accurately and therefore to understand fully the importance of the SS^{min} and SS^{max} in natural magmas. However, numerous experimental and modelling studies have demonstrated the SS^{min} at the f_{O2} range relevant to abundant terrestrial magma types (e.g., Fincham and Richardson 1954; Katsura and Nagashima 1974; Carroll and Rutherford 1985; Moretti *et al.* 2003; Clemente *et al.* 2004; Backnaes and Deubener 2011; Lesne *et al.* 2015; Matjuschkin *et al.* 2016; Nash *et al.* 2019). When these experimental results are combined with our model results, this phenomenon is likely to play a role in magmatic and volcanic processes affecting terrestrial magmas. We explore the influence of the SS^{min} and SS^{max} in experiments ("Solubility experiments") and in natural processes and describe its possible application as a tool for constraining magmatic f_{O2} ("Using w^m_{ST} as an oxybarometer"). These potential impacts on natural magmatic systems are summarised schematically in Figure 1c. We highlight natural processes throughout the magmatic and volcanic system, starting deep with mantle melting ("Mantle melting"); up through the crust where magmas undergo mixing ("Magma mixing and crustal assimilation") and degassing ("Magma ascent and degassing"); and finally to volcanic emissions into the atmosphere ("Volcanic emissions").

Solubility experiments

The SS^{min} and SS^{max} described in "Independent variables of T, f_{O2}, f_{S2}, w^m_{ST}, P, μ_{FeS}, and μ_{CaSO4}" have been observed in experiments that can externally control P, T, f_{O2}, and f_{S2}. For example, the SS^{min} has been observed using one-atmosphere gas-mixing experiments at constant T and P with varying f_{O2} (e.g., Fincham and Richardson, 1954; Katsura and Nagashima, 1974). In these experiments, f_{S2} was *not* constant as the volume percentage of SO_2 in the gas prior to heating in the gas mixing furnace was constant instead, which was mixed with other gas species to attain the required f_{O2}. Despite the more complex gas speciation of such experiments, and that the systems were not simple ternaries, the geometry of w^m_{ST} vs. f_{O2} are reproduced by our modelling (e.g., compare Figure 2a in Fincham and Richardson (1954) with our silm, silicate melt; v, vapour; $sulf^m$, sulfide melt; anh, anhydrite; P^v_{sat}, pressure of vapour-saturation; f_{O2}, oxygen fugacity; w^m_{ST}, total dissolved S content of the silicate melt.

Figure 2e). Consistent with our analysis ("Regions with mixed speciation in the silicate melt or vapour"), Fincham and Richardson (1954) attributed the first change in slope in their Figure 2a to a change in vapour speciation and the second to change in silicate melt speciation. At constant T and P, a different f_{S2}-f_{O2} path can be followed in one-atmosphere gas-mixing experiments using the bulk composition of the input gas to control f_{S2} as well as f_{O2} (e.g., O'Neill and Mavrogenes 2002; Nash *et al.* 2019). O'Neill and Mavrogenes (2002) did not observe an SS^{min} because the f_{O2} was always lower than the expected value of $^{SSmin}f_{O2}$, but Nash *et al.* (2019) did observe an SS^{min} (although not the change in slope due to changes in vapour speciation).

Piston cylinder experiments by Matjuschkin et al. (2016) produced an SS^{min} in (sulfide melt + vapour)-saturated silicate melts at constant P and T, in which f_{O2} was controlled using solid-state buffers (their Figure 8b). Their experiments were always saturated with sulfide melt (except one set at very high f_{O2} that were anhydrite-saturated), whereas the minimum described in "Silicate melt + (vapour and/or sulfide melt and/or anhydrite)" (ε in

Figure 6e) is only vapour-saturated (i.e., it is *not* sulfide melt-saturated). Matjuschkin et al. (2016) attributed their SS^{min} to the presence of an additional S-bearing melt species with intermediate charge between 2- and 6+ that was not quenchable. Alternatively, their minimum could be influenced by a decrease in S^{2-}CSS reflecting compositional changes in the silicate melt due to crystallisation as f_{O2} varied.

A variety of studies using high-pressure, high-temperature apparatus at constant T and P and varying f_{O2} have observed an increase in w^m_{ST} as the system transitioned from sulfide melt- to anhydrite-saturation (e.g., Carroll and Rutherford 1985, 1987; Jugo *et al.* 2004; Beermann *et al.* 2011; Botcharnikov *et al.* 2011). However, these studies suggested a plateau rather than a maximum, likely due to the narrow f_{O2} range of the SS^{max}. However, Jugo (2009) modelled the data from Carroll and Rutherford (1985, 1987) and Jugo *et al.* (2004) and produced an SS^{max} similar to what we have described in "Silicate melt + (vapour and/or sulfide melt and/or anhydrite)" (although they did not consider vapour-saturation as an additional constraint). It is encouraging that our calculated trends match Figure 1 from Jugo (2009), despite using different sets of equations, solubility mechanisms, and thermochemical parameters.

Mantle melting

The SS^{max} we have described defines the maximum S content for silicate melts generated by partial mantle melting (i.e., in the presence of sulfide melt + anhydrite ± vapour at a given T). Once either

sulfide melt or anhydrite is exhausted, the S content of the partial melt decreases to w^m_{STCAS} or w^m_{STCSS}, respectively, and then decreases further by dilution when both phases are exhausted (e.g., Chowdhury and Dasgupta, 2019). Chowdhury and Dasgupta (2019) explored the S content of silicate melts generated by mantle melting when the mantle contains either sulfide or anhydrite. They found that the S content of most arc magmas could be generated by mantle melting in the presence of sulfide when S^{2-} is the dominate silicate melt species. For some arc magmas, they found this was not the case, but sulfide should still be present in the mantle source during melting. They attributed these higher S contents to the presence of sulfate in the silicate melt: this can be visualised in Figure 6c by partial mantle melting producing silicate melts between the dashed green vertical lines. For two of their arc magmas, the S concentrations were too high for even anhydrite-saturated melting, which Chowdhury and Dasgupta (2019) suggested requires an additional S source, such as crustal assimilation of sulfate. Alternatively, our modelling suggests these S-rich magmas could be generated by melting of mantle sources containing both sulfide and anhydrite (or with only one of these phases but at an f_{O2} close to SS^{max}), since this would result in w^m_{ST} of the silicate partial melt higher than S^{6+}CAS. However, a thorough assessment requires knowledge of the T and melt composition dependence of C_{S6+} to model mantle melting. The presence of mixed S speciation in the melt also means melting from sulfide- or anhydrite-bearing mantle can generate a wide range of S concentrations in the silicate melt (e.g., Jugo, 2009).

Magma mixing and crustal assimilation

In nature, approximately constant P paths could be important when mixing reduced and oxidised S-bearing silicate melts. For example, mixing vapour-undersaturated silicate melts from either side of $^{SSmin}f_{O2}$ would generate a vapour-saturated silicate melt if the combined S content is greater than w^m_{ST} at the intermediate f_{O2}, which can be visualised using Figure 7g. At P = 550 bar (black dashed horizontal line), both a relatively reduced (white circle at 3.26 wt% O_2) and oxidised (white square at 4.23 wt% O_2) silicate melt containing 5000 ppm w^m_{ST} would be vapour-undersaturated (Figure 7c). Mixing these silicate melts isobarically results in a new bulk composition between the two end members in Figure 7 that depends on the mixing proportions. If the mixed silicate melt has a bulk composition inside the vapour-saturation curve for 5000 ppm S_T (i.e., the black curve; between $+1.0 \lesssim \Delta FMQ \lesssim +1.7$ for the example shown in Figure 7g), the silicate melt will become vapour-saturated (Figure 7f). The mixed magma will then degas until w^m_{ST} decreases to the contour at that point (Figure 7c) and the amount of vapour degassed will depend on the mixing proportions (Figure 7e). This simple analysis assumes the oxidized and reduced silicate melts are the same in composition (other than in total O_2). If they differ in major element chemistry or T, there would be added complexity because C_{S2-}, C_{S6+}, and T will change depending on the proportions of the two silicate melts in the mixture (and the possibility of crystallization of the mixture). These factors would also influence the solubility of S as a function of the mixing proportions of the two silicate melts. This would be particularly important if a reduced silicate melt assimilated oxidised country rock or an oxidised silicate melt assimilated reduced country rock (e.g., Tomkins *et al.* 2012; Iacono-Marziano *et al.* 2017). Nevertheless, encountering SS^{min} during mixing could be relevant to eruptive dynamics and volcanic SO_2 contributions to the atmosphere by rapidly producing a large amount of vapour (e.g., Figure 7e), potentially driving eruption (e.g., Kress 1997; Di Muro *et al.* 2008). It could also lead to deeper degassing, wringing out S-rich gas at higher P than would occur if the magmas in the mixture had erupted without mixing (see "Magma ascent and degassing").

Magma ascent and degassing

For vapour-saturated magma ascent to the surface, P and bulk composition are two key independent variables. Our calculations for the model ternary system show that f_{O2} paths during isothermal depressurisation of a representative Hawaiian basalt are unlikely to cross ${}^{SSmin}f_{O2}$ (Figure 7d and Figure 8b; "Isothermal, decompression-induced degassing"). Thus, in this system, w^m_{ST} decreases monotonically with decreasing P for a closed- (and open-) system once vapour-saturation is reached (Figure 7c and Figure 8c). In this simple system at low P, this is expected because the partial molar volumes of the gaseous S-bearing species are higher than those of the dissolved silicate melt species. Hence, the progressively more degassed state is the more stable one with decreasing P (i.e., a stable isothermal system requires that volume increases as P decreases so that the bulk isothermal compressibility is always positive). We have not evaluated the possible effects of changes in T or silicate melt composition during degassing (e.g., due to crystallization resulting from heat loss and/or from an increase in the liquidus on degassing). These changes would result in changes in C_{S2-} and/or C_{S6+} and therefore the value of ${}^{SSmin}f_{O2}$ at a particular P could vary during degassing, possibly resulting in SS^{min} influencing w^m_{ST} during degassing.

Degassing of C- and H-bearing species from a silicate melt can cause f_{O2} to increase (e.g., Sato and Wright 1966; Sato 1978; Mathez 1984; Candela 1986; Holloway 2004; Burgisser and Scaillet 2007; Brounce *et al.* 2017; Métrich 2021). The magnitude of this f_{O2} increase is greater when the initial f_{O2} of the magma is lower and depends on the relative solubilities of oxidised and reduced C- and H-bearing silicate melt species (e.g., Gaillard *et al.* 2015). Therefore, it may be possible to have a vapour-saturated silicate melt that starts S^{2-}-dominated but oxidises sufficiently due to early CO_2 and/or H_2O degassing to drive the system across SS^{min} during depressurisation. If so, this could be manifested by initially decreasing, followed by increasing, w^m_{ST} with progressive closed-system, depressurisation-induced degassing. It is also possible that a maximum in w^m_{ST} could occur during degassing, although this would not be due to changes in f_{O2} or the SS^{min}. For example, the loss of CO_2 and H_2O prior to significant S degassing could cause w^m_{ST} to initially increase (i.e., because the total mass of the silicate melt is decreasing while the mass of dissolved S is nearly constant); then, when S begins to degas, w^m_{ST} would decrease.

Progressive reduction or oxidation of magmas during degassing is expected based on previous modelling efforts and has been observed in natural samples (e.g., Anderson and Wright 1972; Candela 1986; Carmichael and Ghiorso 1986; Burgisser and Scaillet 2007; Métrich *et al.* 2009; Gaillard *et al.* 2011, 2015; Kelley and Cottrell 2012; Moussallam *et al.* 2016, 2014; Brounce *et al.* 2017). Our degassing calculations demonstrate that the f_{O2} after extensive S-degassing will not represent the initial silicate melt unless the silicate melt began degassing near SS^{min} (Figure 7d). For example, when f_{O2} differs from that of ${}^{SSmin}f_{O2}$ (i.e., at the diamond) by more than ~0.1 log unit (either positively or negatively), the f_{O2} after nearly complete degassing (i.e., P =1 bar) has increased or decreased by more than 0.5 log units (and up to > 1 log unit) relative to the initial (i.e., undegassed) f_{O2} of the silicate melt (Figure 7d). Therefore, as has been highlighted previously, using the f_{O2} of volcanic gases (or from the Fe^{3+}/Fe_T or S^{6+}/S_T of silicate glasses) as a proxy for the f_{O2} of the initial silicate melt (and potentially of the mantle), should be approached with caution (e.g., Anderson and Wright 1972; Carmichael and Ghiorso 1986; Burgisser and Scaillet 2007; Métrich *et al.* 2009; Gaillard *et al.* 2015). We emphasize, however, that the direction of the change in f_{O2} on degassing differs for more oxidized and reduced magmas relative to ${}^{SSmin}f_{O2}$ (Figure 7d and Figure 8b).

The unlikelihood of crossing the SS^{min} during closed- or open-system degassing does not mean that SS^{min} is unimportant during degassing. Decompression paths to the left and right of SS^{min} begin to degas at lower P than one that passes right through the maximum (Figure 7c). The shapes of the contours in Figure 7c are simple expressions of the SS^{min} described in "Silicate melt + vapour" for the case $Y = w^m_{ST}$ (Figure 2d and Figure 4c). The maximum in P at the SS^{min} is occurs because a higher P is required to keep a given concentration of S dissolved in the silicate melt (5000 ppm in Figure 7c) at the SS^{min} than when the S solubility is higher on either side. Based on our modelling, a Hawaiian basaltic melt with 5000 ppm S_T reaches vapour-saturation at 666 bars at SS^{min} (the green curve in Figure 8). This is 164 bars higher than when the melt is initially 0.5 log units higher in f_{O2} (the turquoise curve) and 363 bars higher than when the melt is initially 0.6 log units lower in f_{O2} (the yellow curve). Thus, SS^{min} can exert significant control on the P at which S degassing begins as a function of f_{O2} (Figure 7). Therefore, even for S-rich magmas, S will degas only at shallow depths if the silicate melt has an initial f_{O2} sufficiently lower than (e.g., MORB) or higher than ${}^{SSmin}f_{O2}$. However, silicate melts with initial f_{O2} close to ${}^{SSmin}f_{O2}$ (e.g., many arc and OIB magmas) would – all other things being equal – begin to degas S deeper than more oxidized or reduced magmas. Therefore, the SS^{min} could be a contributing mechanism – in addition to S partitioning into the H_2O-rich vapour exsolved from H_2O-rich magmas (e.g., Wallace and Edmonds 2011; Zajacz *et al.* 2012; Edmonds and Mather 2017; Edmonds and Woods 2018) – for the deep degassing of S in arc and some ocean island settings.

The SS^{min} also has implications for calculating the P^v_{sat} using the volatile concentrations of glasses (e.g., in pillow rims and glassy melt inclusions) (e.g., Anderson *et al.* 1989; Blundy and Cashman 2008). Such calculated pressures are often used to constrain the architecture of magmatic systems and link volcanic products to eruptive vents in submarine systems. These calculations are based on generalisations of equation (7) that include other gaseous species for which partial pressures can be determined (e.g., CO_2 and H_2O). This exercise is comparable to when T, f_{O2}, and $Y = w^m_{ST}$ are taken as independent variables in a silicate melt + vapour assemblage and the dependent variable $Z = P$ is calculated (e.g., Figure 4c). The effect of dissolved S is currently not included in such calculations, which include only H_2O and CO_2 (e.g., Newman and Lowenstern 2002; Papale *et al.* 2006; Iacono-Marziano *et al.* 2012; Ghiorso and Gualda 2015; Allison *et al.* 2019; Iacovino *et al.* 2021). Also, the effect f_{O2} on volatile speciation in the silicate melt and vapour is mostly ignored (but see Scaillet and Pichavant 2004; Wetzel *et al.* 2015).

MORB magmas have $S^{6+}/S_T < 0.05$ (e.g., Métrich *et al.* 2009; Jugo *et al.* 2010; Labidi *et al.* 2012) and therefore including S for such melts would have a negligible effect on calculated P^v_{sat} because p_{S2} and p_{SO2} would be low (e.g., Figure 2d). However, OIB and arc volcanic glasses can have $[S^{6+}/S_T]^m$ up to 1 (e.g., Jugo *et al.* 2010; de Moor *et al.* 2013; Labidi *et al.* 2015; Muth and Wallace 2021), and therefore the effects of the SS^{min} on the contribution of partial pressures from S-bearing species to the total P at vapour-saturation (e.g., S_2 and SO_2 in the S–O system, but potentially H_2S and OCS as well in C–O–H–S system) could be non-negligible (e.g., in the green band of Figure 2d). Melt inclusions from arc and OIB magmas reach $w^m_{ST} \sim 5000$ ppm (Wallace 2005) and are ΔFMQ-3 to +3 (Cottrell *et al.* 2021), which could lead to underestimating P^v_{sat} by up to 650 bars for melts at ΔFMQ = +1 to +2 (Figure 9). The exact value of the underestimate would depend on the f_{O2}, C_{S6+}, and C_{S2}, and hence T and silicate melt composition, and including the H and C species (e.g., Burgisser *et al.* 2015; Lesne *et al.* 2015; Hughes *et al.* 2021). However, the potential magnitude of this SS^{min}-related effect implied by our calculations is robust. Therefore,

in such cases neglecting S could result in calculated P^{v}_{sat} values that significantly underestimate the P^{v}_{sat} the glass is recording.

We note that the maximum in P^{v}_{sat} at SS^{min} based on our calculations contrasts with the modelling of Lesne *et al.* (2015), who predict a *minimum* in P^{v}_{sat} when both reduced and oxidised S species are present in silicate melts. The difference could be due to: (1) different assumptions regarding the speciation of oxidised S in the silicate melt (i.e., as SO_2 rather than SO_4^{2-}; see "Equilibria between silicate melt, vapour, sulfide melt, and anhydrite" for discussion of potential S-bearing species in the silicate melt); and (2) the effect of H on the SS^{min}, which adds H_2S species to the silicate melt and vapour.

Volcanic emissions

The El Chichón 1982 and Pinatubo 1991 eruptions released the largest quantities of SO_2 during explosive events recorded by satellites, and most of this SO_2 was sourced from a coexisting vapour present prior to eruption (e.g., Wallace and Gerlach 1994; Krueger *et al.* 1995; Gerlach *et al.* 1996; Keppler 1999; Bluth *et al.* 2015). Additionally, both magmas contain anhydrite and pyrrhotite/sulfide in the erupted products (e.g., Luhr *et al.* 1984; Bernard *et al.* 1991; Luhr 2008a). We infer from this observation that both these magmas were stored at SS^{max} prior to eruption (i.e., at the condition represented by the grey star in
Figure 5g). Independent f_{O2} estimates from these magmas are within the range for experimental constraints for the coexistence of sulfide melt and anhydrite (e.g., Luhr *et al.* 1984; Rye *et al.* 1984; Carroll and Rutherford 1987; Evans and Scaillet 1997; Luhr 2008b). Older eruptions have released even greater quantities of SO_2 (e.g., Figure 5 in Vidal *et al.* 2016) and these magmas may have also been stored at SS^{max}. For example, eruptive products from the Samalas 1257 eruption contain sulfides and vapour, and anhydrite has been observed as microcrystals on the walls of fluid inclusions (Vidal *et al.* 2016) (although anhydrite dissolves in water and is therefore rarely observed in volcanic products; Luhr *et al.* 1984). These results from older eruptions are consistent with the SS^{max} being connected to unusually large releases of SO_2 during explosive eruptions. If this is correct, it suggests a connection between the unique f_{O2} at which the SS^{max} occurs and these events.

The "petrologic method" is often used to estimate the volatiles emissions from volcanic eruptions by subtracting the volatile concentration of the degassed matrix glass from that in melt inclusions (the latter is assumed to represent undegassed silicate melt) (e.g., Devine *et al.* 1984; Thordarson *et al.* 1996; Wallace 2001; Sharma *et al.* 2004). The total SO_2 emitted during eruption estimated in this way are often low relative to those measured using other techniques (e.g., satellite-based techniques; e.g., Stoiber and Jepsen 1973; Rose *et al.* 1982; Andres *et al.* 1991; Wallace 2001; Shinohara 2008). This "excess sulfur" problem reflects the large amounts of SO_2-rich vapour often present during magma storage (only minor amounts of SO_2 are thought to be released from the break-down of sulfide melt and anhydrite during degassing) (e.g., Anderson 1975; Luhr *et al.* 1984; Andres *et al.* 1991; Wallace and Gerlach 1994; Gerlach and McGee 1994; Gerlach *et al.* 1994, 1996; Giggenbach 1996; Keppler 1999; Wallace 2001; Scaillet and Pichavant 2003; Scaillet *et al.* 2003; Sharma *et al.* 2004; Shinohara 2008). Large amounts of S-rich vapour could be generated due to the SS^{min} (and to some extents SS^{max}). Therefore, using glass-only melt inclusions trapped at SS^{min} or SS^{max} will result in the largest discrepancies with other methods due to the additional S in other phases. Melt inclusions that co-entrap these additional phases cannot be used because the proportions of the different phases present in the inclusion are unlikely to represent

the bulk system. Additionally, as melt inclusions evolve as a closed-system to S post-entrapment, SS^{min} and SS^{max} may be encountered causing additional phases to form within the inclusion (e.g., vapour bubbles, sulfide blebs). Measuring only the silicate glass within these melt inclusion results in a greater underestimate of SO_2 emissions because the S contribution from the silicate melt is additionally underestimated (e.g., Venugopal *et al.* 2020).

Using w^m_{ST} as an oxybarometer

For a silicate melt with a given value of w^m_{ST} and T, it is possible to place constraints on its f_{O2} using the calculations we have presented based on the presence or absence of vapour, sulfide melt, and/or anhydrite as saturating phases (
Figure 6; e.g., the empirical approach of Beermann et al., 2011). Suppose it is known that the silicate melt is vapour-saturated. If it is also saturated with sulfide melt it must fall on the solid grey $sulf^m$ curve in
Figure 6a: so for a known w^m_{ST}, the f_{O2} can be read directly from the $sulf^m$ curve (e.g., α and β for 3000 and 13000 ppm w^m_{ST}, respectively, in
Figure 6a). Likewise, if the silicate melt is known to be anhydrite-saturated it must fall on the dashed grey *anh* curve in
Figure 6a: the implied f_{O2} for a given value of w^m_{ST} can be read from the *anh* curve (e.g., γ for 13000 ppm w^m_{ST} in
Figure 6a). If the silicate melt is known to be saturated with both sulfide melt and anhydrite, the f_{O2} is constrained to the SS^{max} value at the grey star.

Suppose, however, that we do not know whether the vapour-saturated silicate melt is sulfide melt and/or anhydrite saturated (or we know that it is not). Then the f_{O2} can be constrained to be between the $sulf^m$ and *anh* curves in
Figure 6a for a given value of w^m_{ST} (e.g., at 13000 ppm w^m_{ST}, the f_{O2} must be between β and γ on
Figure 6a). When nearly all of the dissolved S is S^{2-} (i.e., in the purple-blue-turquoise region), the $sulf^m$ curve plateaus at ~w^m_{S2-CSS}, so for values of $w^m_{ST} < w^m_{S2-CSS}$, no constraint can be placed on a lower bound to f_{O2} using this approach. Likewise, the *anh* curve plateaus at ~w^m_{S6+CAS}, and thus no constraint on an upper bound on f_{O2} can be determined by this approach if $w^m_{ST} < w^m_{S6+CAS}$. If the silicate melt is not thought to be vapour-saturated, but P is known independently, a figure like
Figure 6c at the relevant P can be used instead. Although the presence of other volatiles (e.g., C and H) will modify the results from the simple S–O system, the principles are the same.

The technique described using
Figure 6a is most sensitive when measured S concentrations are high and the S speciation in the silicate melt is mixed (ΔFMQ ~ +1 to +2); e.g., to obtain both lower and upper bounds on f_{O2} in the example described requires $w^m_{ST} > w^m_{S6+CAS}$ ~13000 ppm (i.e., the white dotted line in
Figure 6a). Although this is much higher than the typical total dissolved S contents of common magmas, $S^{6+}CAS$ decreases significantly with increasing dissolved H_2O and decreasing T: e.g., $S^{6+}CAS$ = ~3000 ppm at 5 wt% H_2O and 1200 °C for a basaltic melt (Chowdhury and Dasgupta 2019). Melt inclusions from arcs and ocean islands can be S-rich (up to ~5000 ppm S_T), hydrous (up to ~6 wt% H_2O for arcs and ~3 wt% H_2O for ocean islands), and relatively oxidised (up to +3 ΔFMQ) (e.g., Wallace 2005; Moussallam *et al.* 2019; Cottrell *et al.* 2021) and may therefore

provide useful f_{O2} estimates based on this technique. However, this will require accurate knowledge of C_{S2-}, C_{S6+}, S^{2-}CSS, and S^{6+}CSS at the relevant conditions (especially the effects of T and silicate melt composition – including the influence of H_2O), as these parameters strongly influence the f_{O2} of the transition from S^{2-}- to S^{6+}-dominated silicate melt (e.g., O'Neill and Mavrogenes 2002, 2019; Li and Ripley 2005; Moretti and Ottonello 2005; Baker and Moretti 2011; Chowdhury and Dasgupta 2019; Nash *et al.* 2019; Zajacz and Tsay 2019; O'Neill 2020; Boulliung and Wood 2021).

Conclusions

Depending on the choice of independent variables, vapour-saturated silicate melts can with increasing f_{O2} encounter a "sulfur solubility minimum" (SS^{min}) when both S^{2-} and S^{6+} are dissolved in the silicate melt in similar concentrations (Figure 2–Figure 5). This occurs because O_2 is on different sides of the reactions describing S^{2-} and S^{6+} dissolution in the silicate melt from S_2- and/or SO_2-dominant vapour (e.g., reactions (4a) and (5a)). Examples of choices of independent variables and the paths they follow that exhibit a minimum in the dissolved total S content (w^m_{ST}) in vapour-saturated silicate melt include paths of increasing f_{O2} for which T and either f_{S2} or P are held constant (

Figure 3c and

Figure 5c). For paths on which w^m_{ST} is held constant with increasing f_{O2} and constant T, the SS^{min} is expressed a maximum in P (Figure 4c). However, not all choices of independent variables or paths defined by changes in these variables display the SS^{min}. An important geological example of this is that despite changing f_{O2}, w^m_{ST} decreases monotonically (i.e., no minimum in w^m_{ST} is encountered) during isothermal, closed-system, decompression-induced degassing in a system in which the vapour contains only S- and O-bearing species (Abbreviations: sil^m, silicate melt; v, vapour; $sulf^m$, sulfide melt; anh, anhydrite; MORB, mid-ocean ridge basalts; OIB, ocean island basalts; and Arc, arc basalts.
Figure 7c).

There is also a maximum in w^m_{ST} (SS^{max}) of silicate melts that are multiply-saturated with sulfide melt and anhydrite at fixed T, and a global maximum if vapour is also present. Like the SS^{min}, this SS^{max} also occurs at an f_{O2} value at which both S^{2-} and S^{6+} are dissolved in the silicate melt in similar concentrations (

Figure 5g). This maximum can be explained by the constraints of sulfide melt- and anhydrite-saturation leading to simultaneous maximization of the concentrations of both the S^{2-} and S^{6+} species in the silicate melt. Additionally, P and f_{O2} are dependent variables at SS^{max} once the independent conditions of constant T, sulfide melt-saturation (which sets the value of μ_{FeS}), and anhydrite-saturation (which sets μ_{CaSO4}) are imposed. A maximum in w^m_{ST} is also encountered at constant T with increasing f_{O2} when a vapour-undersaturated silicate melt is both sulfide melt- and anhydrite-saturated (

Figure 6c).

These SS^{min} and SS^{max} features can play important roles over the entire magmatic and volcanic system, extending from the mantle to eruption (Figure 1c). However, their influences depends on the independent variables governing the system at each point during the process, the paths followed by these variables, and their effects on dependent parameters. For example, these features can

influence the maximum S concentration in mantle melts; the volatile release from magma mixing and crustal assimilation; the depth that significant amounts of S begin to degas from silicate melt; the f_{O2} of erupted magma and emissions of volcanic gases; and the amounts of SO_2 released to the atmosphere during explosive eruptions. Additionally, they may also impact some of the tools used to infer intensive and extensive variables of these systems. Excluding the effects of the SS^{min} (and SS^{max}) can cause significant underestimations in calculations of P^{v}_{sat}, as well as SO_2 emissions using the petrologic method. SS^{max} also provides the possibility of constraining f_{O2} for S-bearing magmas based on limits set by the f_{O2} dependence of w^{m}_{ST} of silicate melts saturated with vapour, sulfide melt, and/or anhydrite.

We emphasize that our approach has been to use a simplified ternary system (silicate–O_2–S_2) to model thermodynamically the coexistence of silicate melt + (vapour and/or sulfide melt and/or anhydrite). This choice allows us to isolate and analyse the interplay of key variables in a system in which all the volatile species in the vapour are on the S-O join. Therefore, we have not included the effects of other volatile components that typically make up most of the gas phase. Although we are confident that the patterns and behaviour expressed in this simple system can be generalized to natural systems, an important next step will be to include other components and species in the silicate melt and vapour. Our approach can be readily expanded to model such complex natural systems, particularly when H and C are present. Principally, this involves including additional species and homogeneous equilibria to the vapour (e.g., H_2, H_2O, CO, CO_2, CH_4, H_2S, OCS, etc.) and solubility reactions for the species that dissolve in the silicate melt (e.g., OH^-, H_2O, H_2, CO_3^{2-}, CO_2, CO, CH_4, H_2S, SH^- etc.). Full generalization of our results to natural systems will require exploring the effects of variations in composition on solubility and speciation (e.g., the composition of the silicate melt, including H_2O and $[Fe^{3+}/Fe_T]^m$) and the P and T dependence of the equilibrium constants for heterogenous silicate melt-vapour equilibria. This is currently of particular importance for the sulfate capacity (C_{S6+}), which controls the behaviour of dissolved sulfate and is expected to be strongly influenced by T and melt composition (e.g., Moretti and Ottonello 2005; Nash *et al.* 2019; O'Neill and Mavrogenes 2019; Boulliung and Wood 2021; Moretti 2021). Although such an expanded treatment will be important and useful in detailed modelling of natural systems, the complexity already present in our simple system – for a single Hawaiian basaltic melt composition in which only S ± O-bearing species are included – highlights in our view the importance of adding complexity (especially in terms of silicate melt and vapour composition) incrementally to such end member systems for understanding the behaviour of sulfur in magmatic systems.

Funding

ECH was funded by a Caltech Geology Option Post-Doctoral Fellowship and a Caltech Centre for Comparative Planetary Evolution (^{3}CPE) research grant, and is supported by the Hazards and Risk Management Programme, which is part of New Zealand Strategic Science Investment Funding (SSIF) from the New Zealand Ministry of Business, Innovation & Employment (MBIE). PL is funded by an Embiricos Trust scholarship from Jesus College, University of Cambridge.

Conflict of interest

The authors declare no known conflicts of interest associated with this publication.

Author contributions

ECH, EMS, and LS conceived the project idea. ECH wrote the code with the help of PL. ECH ran the analyses. ECH and EMS led manuscript production, with further contribution from LS and PL.

References

Allison, C.M., Roggensack, K. and Clarke, A.B. 2019. H2O–CO2 solubility in alkali-rich mafic magmas: new experiments at mid-crustal pressures. *Contributions to Mineralogy and Petrology*, **174**, 58, https://doi.org/10.1007/s00410-019-1592-4.

Anderson, A.T. 1975. Some basaltic and andesitic gases. *Reviews of Geophysics*, **13**, 37–55, https://doi.org/10.1029/RG013I001P00037.

Anderson, A.T. and Wright, T.L. 1972. Phenocrysts and glass inclusions and their bearing on oxidation and mixing of basaltic magmas, kilauea volcano, hawaii. *American Mineralogist*, **57**, 188–216.

Anderson, A.T.J., Newman, S., Williams, S.N., Druitt, T.H., Skirius, C. and Stolper, E. 1989. H2O, CO2, CI, and gas in Plinian and ash-flow Bishop rhyolite | Geology | GeoScienceWorld. *Geology*, **17**, 221–225.

Andres, R.J., Rose, W.I., Kyle, P.R., DeSilva, S. and Francis, P. 1991. Excessive sulfur dioxide emissions from Chilean volcanoes. *Journal of Volcanology and Geothermal Research*, **46**, 323–329.

Backnaes, L. and Deubener, J. 2011. Experimental studies on sulfur solubility in silicate melts at near-atmospheric pressure. *Reviews in Mineralogy and Geochemistry*, **73**, 143–165, https://doi.org/10.2138/rmg.2011.73.6.

Baker, D.R. and Moretti, R. 2011. Modeling the Solubility of Sulfur in Magmas: A 50-Year Old Geochemical Challenge. *Reviews in Mineralogy and Geochemistry*, **73**, 167–213, https://doi.org/10.2138/RMG.2011.73.7.

Baumgartner, R.J., Baratoux, D., Gaillard, F. and Fiorentini, M.L. 2017. Numerical modelling of erosion and assimilation of sulfur-rich substrate by martian lava flows: Implications for the genesis of massive sulfide mineralization on Mars. *Icarus*, **296**, 257–274, https://doi.org/10.1016/j.icarus.2017.06.016.

Beermann, O., Botcharnikov, R.E., Holtz, F., Diedrich, O. and Nowak, M. 2011. Temperature dependence of sulfide and sulfate solubility in olivine-saturated basaltic magmas. *Geochimica et Cosmochimica Acta*, **75**, 7612–7631, https://doi.org/10.1016/j.gca.2011.09.024.

Bernard, A., Demaiffe, D., Mattielli, N. and Punongbayan, R.S. 1991. Anhydrite-bearing pumices from Mount Pinatubo: further evidence for the existence of sulphur-rich silicic magmas. *Nature 1991 354:6349*, **354**, 139–140, https://doi.org/10.1038/354139a0.

Blundy, J.D. and Cashman, K.V. 2008. Petrologic reconstruction of magmatic system variables and processes. *Reviews in Mineralogy and Geochemistry*, **69**, 179–239.

Bluth, G.J.S., Rose, W.I., Sprod, I.E. and Krueger, A.J. 2015. Stratospheric Loading of Sulfur From Explosive Volcanic Eruptions. *https://doi.org/10.1086/515972*, **105**, 671–683, https://doi.org/10.1086/515972.

Botcharnikov, R.E., Linnen, R.L., Wilke, M., Holtz, F., Jugo, P.J. and Berndt, J. 2011. High gold concentrations in sulphide-bearing magma under oxidizing conditions. *Nature Geoscience*, **4**, 112–115, https://doi.org/10.1038/ngeo1042.

Boulliung, J. and Wood, B.J. 2021. Temperature and melt composition effects on sulfate solubility in silicate melts at atmospheric pressure. *In*: *Goldschimdt Conference Abstracts*.

Brounce, M.N., Stolper, E.M. and Eiler, J. 2017. Redox variations in Mauna Kea lavas, the oxygen fugacity of the Hawaiian plume, and the role of volcanic gases in Earth's oxygenation. *Proceedings of the National Academy of Sciences of the United States of America*, **114**, https://doi.org/10.1073/pnas.1619527114.

Burgisser, A. and Scaillet, B. 2007. Redox evolution of a degassing magma rising to the surface. *Nature*, **445**, 194–197, https://doi.org/10.1038/nature05509.

Burgisser, A., Alletti, M. and Scaillet, B. 2015. Simulating the behavior of volatiles belonging to the C–O–H–S system in silicate melts under magmatic conditions with the software D-Compress. *Computers & Geosciences*, **79**, 1–14, https://doi.org/10.1016/J.CAGEO.2015.03.002.

Candela, P.A. 1986. The evolution of aqueous vapor from silicate melts: Effect on oxygen fugacity. *Geochimica et Cosmochimica Acta*, **50**, 1205–1211, https://doi.org/10.1016/0016-7037(86)90403-5.

Carmichael, I.S.E. and Ghiorso, M.S. 1986. Oxidation-reduction relations in basic magma: a case for homogeneous equilibria. *Earth and Planetary Science Letters*, **78**, 200–210, https://doi.org/10.1016/0012-821X(86)90061-0.

Carroll, M.R. and Rutherford, M.J. 1985. Sulfide and sulfate saturation in hydrous silicate melts. *Journal of Geophysical Research: Solid Earth*, **90**, C601–C612, https://doi.org/10.1029/JB090IS02P0C601.

Carroll, M.R. and Rutherford, M.J. 1987. The Stability of Igneous Anhydrite: Experimental Results and Implications for Sulfur Behavior in the 1982 El Chichon Trachyandesite and Other Evolved Magmas. *Journal of Petrology*, **28**, 781–801, https://doi.org/10.1093/PETROLOGY/28.5.781.

Chowdhury, P. and Dasgupta, R. 2019. Effect of sulfate on the basaltic liquidus and Sulfur Concentration at Anhydrite Saturation (SCAS) of hydrous basalts – Implications for sulfur cycle in subduction zones. *Chemical Geology*, **522**, 162–174, https://doi.org/10.1016/J.CHEMGEO.2019.05.020.

Clemente, B., SCAILLET, B. and PICHAVANT, M. 2004. The Solubility of Sulphur in Hydrous Rhyolitic Melts. *Journal of Petrology*, **45**, 2171–2196, https://doi.org/10.1093/petrology/egh052.

Colin, A., Schmidt, C., Pokrovski, G.S., Wilke, M., Borisova, A.Y. and Toplis, M.J. 2020. In situ determination of sulfur speciation and partitioning in aqueous fluid-silicate melt systems. *Geochemical Perspectives Letters*, 31–35, https://doi.org/10.7185/GEOCHEMLET.2020.

Cottrell, E., Birner, S.K., Brounce, M., Davis, F.A., Waters, L.E. and Kelley, K.A. 2021. Oxygen Fugacity Across Tectonic Settings. *In*: Moretti, R. and Neuville, D. R. (eds) *Magma Redox Geochemistry*. 33–61., https://doi.org/10.1002/9781119473206.CH3.

de Moor, J.M., Fischer, T.P., et al. 2013. Sulfur degassing at Erta Ale (Ethiopia) and Masaya (Nicaragua) volcanoes: Implications for degassing processes and oxygen fugacities of basaltic systems. *Geochemistry, Geophysics, Geosystems*, **14**, 4076–4108, https://doi.org/10.1002/ggge.20255.

Devine, J.D., Sigurdsson, H., Davis, A.N. and Self, S. 1984. Estimates of sulfur and chlorine yield to the atmosphere from volcanic eruptions and potential climatic effects. *Journal of Geophysical Research: Solid Earth*, **89**, 6309–6325, https://doi.org/10.1029/JB089IB07P06309.

Di Muro, A., Pallister, J., Villemant, B., Newhall, C., Semet, M., Martinez, M. and Mariet, C. 2008. Pre-1991 sulfur transfer between mafic injections and dacite magma in the Mt. Pinatubo

reservoir. *Journal of Volcanology and Geothermal Research*, **175**, 517–540, https://doi.org/10.1016/J.JVOLGEORES.2008.02.025.
Edmonds, M. and Mather, T.A. 2017. Volcanic Sulfides and Outgassing. *Elements*, **13**, 105–110, https://doi.org/10.2113/gselements.13.2.105.
Edmonds, M. and Woods, A.W. 2018. Exsolved volatiles in magma reservoirs. *Journal of Volcanology and Geothermal Research*, **368**, 13–30, https://doi.org/10.1016/J.JVOLGEORES.2018.10.018.
Evans, B.W. and Scaillet, B. 1997. The redox state of Pinatubo dacite and the ilmenite-hematite solvus. *American Mineralogist*, **82**, 625–629, https://doi.org/10.2138/am-1997-5-621.
Fincham, C. and Richardson, F.D. 1954. The behaviour of sulphur in silicate and aluminate melts. *Proceedings of the Royal Society of London. Series A. Mathematical and Physical Sciences*, **223**, 40–62, https://doi.org/10.1098/rspa.1954.0099.
Frost, B.R. 1991. Introduction to oxygen fugacity and its petrologic importance. *Reviews in Mineralogy and Geochemistry*, **25**, 1–9.
Gaillard, F. and Scaillet, B. 2009. The sulfur content of volcanic gases on Mars. *Earth and Planetary Science Letters*, **279**, 34–43, https://doi.org/10.1016/J.EPSL.2008.12.028.
Gaillard, F. and Scaillet, B. 2014. A theoretical framework for volcanic degassing chemistry in a comparative planetology perspective and implications for planetary atmospheres. *Earth and Planetary Science Letters*, **403**, 307–316, https://doi.org/10.1016/j.epsl.2014.07.009.
Gaillard, F., Scaillet, B. and Arndt, N.T. 2011. Atmospheric oxygenation caused by a change in volcanic degassing pressure. *Nature*, **478**, 229–232, https://doi.org/10.1038/nature10460.
Gaillard, F., Michalski, J., Berger, G., McLennan, S.M. and Scaillet, B. 2013. Geochemical reservoirs and timing of sulfur cycling on Mars. *Space Science Reviews*, **174**, 251–300, https://doi.org/10.1007/s11214-012-9947-4.
Gaillard, F., Scaillet, B., Pichavant, M. and Iacono-Marziano, G. 2015. The redox geodynamics linking basalts and their mantle sources through space and time. *Chemical Geology*, **418**, 217–233, https://doi.org/10.1016/j.chemgeo.2015.07.030.
Gerlach, T.M. and McGee, K.A. 1994. Total sulfur dioxide emissions and pre-eruption vapor-saturated magma at Mount St. Helens, 1980–88. *Geophysical Research Letters*, **21**, 2833–2836, https://doi.org/10.1029/94GL02761.
Gerlach, T.M., Westrich, H.R., Casadevall, T.J. and Finnegan, D.L. 1994. Vapor saturation and accumulation in magmas of the 1989–1990 eruption of Redoubt Volcano, Alaska. *Journal of Volcanology and Geothermal Research*, **62**, 317–337, https://doi.org/10.1016/0377-0273(94)90039-6.
Gerlach, T.M., Westrich, H.R. and Symonds, R.B. 1996. Preeruption vapor in magma of the climactic Mount Pinatubo eruption: Source of the giant stratospheric sulfur dioxide cloud. *In*: *Fire and Mud: Eruptions and Lahars of Mount Pinatubo, Philippines*.
Ghiorso, M.S. and Gualda, G.A.R. 2015. An H2O–CO2 mixed fluid saturation model compatible with rhyolite-MELTS. *Contributions to Mineralogy and Petrology*, **169**, 53, https://doi.org/10.1007/s00410-015-1141-8.
Giggenbach, W.F. 1996. Chemical Composition of Volcanic Gases. *Monitoring and Mitigation of Volcano Hazards*, 221–256, https://doi.org/10.1007/978-3-642-80087-0_7.
Henley, R.W. and Fischer, T.P. 2021. Sulfur sequestration and redox equilibria in volcanic gases. *Journal of Volcanology and Geothermal Research*, **414**, 107181, https://doi.org/10.1016/J.JVOLGEORES.2021.107181.
Henley, R.W. and Seward, T.M. 2018. Gas–Solid Reactions in Arc Volcanoes: Ancient and

Modern. *Reviews in Mineralogy and Geochemistry*, **84**, 309–349, https://doi.org/10.2138/RMG.2018.84.9.
Holloway, J.R. 2004. Redox reactions in seafloor basalts: possible insights into silicic hydrothermal systems. *Chemical Geology*, **210**, 225–230, https://doi.org/10.1016/J.CHEMGEO.2004.06.009.
Hughes, E.C., Liggins, P., Saper, L. and Stolper, E. 2021. Effect of sulphur and oxygen fugacity on vapour-saturation pressure calculations. *In*: *Goldschmidt*.
Iacono-Marziano, G., Morizet, Y., Le Trong, E. and Gaillard, F. 2012. New experimental data and semi-empirical parameterization of H2O–CO2 solubility in mafic melts. *Geochimica et Cosmochimica Acta*, **97**, 1–23, https://doi.org/10.1016/J.GCA.2012.08.035.
Iacono-Marziano, G., Ferraina, C., Gaillard, F., Di Carlo, I. and Arndt, N.T. 2017. Assimilation of sulfate and carbonaceous rocks: Experimental study, thermodynamic modeling and application to the Noril'sk-Talnakh region (Russia). *Ore Geology Reviews*, **90**, 399–413, https://doi.org/10.1016/J.OREGEOREV.2017.04.027.
Iacovino, K. 2015. Linking subsurface to surface degassing at active volcanoes: A thermodynamic model with applications to Erebus volcano. *Earth and Planetary Science Letters*, **431**, 59–74, https://doi.org/10.1016/J.EPSL.2015.09.016.
Iacovino, K., Matthews, S., Wieser, P.E., Moore, G.M. and Bégué, F. 2021. VESIcal Part I: An open-source thermodynamic model engine for mixed volatile (O-) solubility in silicate melts. *Earth and Space Science*, e2020EA001584, https://doi.org/10.1029/2020EA001584.
Jugo, P.J. 2009. Sulfur content at sulfide saturation in oxidized magmas. *Geology*, **37**, 415–418, https://doi.org/10.1130/G25527A.1.
Jugo, P.J., Luth, R.W. and Richards, J.P. 2004. An Experimental Study of the Sulfur Content in Basaltic Melts Saturated with Immiscible Sulfide or Sulfate Liquids at 1300 C and 1.0 GPa. *Journal of Petrology*, **46**, 783–798, https://doi.org/10.1093/petrology/egh097.
Jugo, P.J., Luth, R.W. and Richards, J.P. 2005. Experimental data on the speciation of sulfur as a function of oxygen fugacity in basaltic melts. *Geochimica et Cosmochimica Acta*, **69**, 497–503.
Jugo, P.J., Wilke, M. and Botcharnikov, R.E. 2010. Sulfur K-edge XANES analysis of natural and synthetic basaltic glasses: Implications for S speciation and S content as function of oxygen fugacity. *Geochimica et Cosmochimica Acta*, **74**, 5926–5938, https://doi.org/10.1016/J.GCA.2010.07.022.
Katsura, T. and Nagashima, S. 1974. Solubility of sulfur in some magmas at 1 atmosphere. *Geochimica et Cosmochimica Acta*, **38**, 517–531, https://doi.org/10.1016/0016-7037(74)90038-6.
Kelley, K.A. and Cottrell, E. 2012. The influence of magmatic differentiation on the oxidation state of Fe in a basaltic arc magma. *Earth and Planetary Science Letters*, **329**–**330**, 109–121, https://doi.org/10.1016/j.epsl.2012.02.010.
Keppler, H. 1999. Experimental evidence for the source of excess sulfur in explosive volcanic eruptions. *Science*, **284**, 1652–1654, https://doi.org/10.1126/SCIENCE.284.5420.1652.
Kress, V. 1997. Magma mixing as a source for Pinatubo sulphur. *Nature 1997 389:6651*, **389**, 591–593, https://doi.org/10.1038/39299.
Krueger, A.J., Walter, L.S., Bhartia, P.K., Schnetzler, C.C., Krotkov, N.A., Sprod, I. and Bluth, G.J.S. 1995. Volcanic sulfur dioxide measurements from the total ozone mapping spectrometer instruments. *Journal of Geophysical Research: Atmospheres*, **100**, 14057–14076, https://doi.org/10.1029/95JD01222.

Labidi, J., Cartigny, P., Birck, J.L., Assayag, N. and Bourrand, J.J. 2012. Determination of multiple sulfur isotopes in glasses: A reappraisal of the MORB δ34S. *Chemical Geology*, **334**, 189–198, https://doi.org/10.1016/J.CHEMGEO.2012.10.028.

Labidi, J., Cartigny, P. and Jackson, M.G. 2015. Multiple sulfur isotope composition of oxidized Samoan melts and the implications of a sulfur isotope 'mantle array' in chemical geodynamics. *Earth and Planetary Science Letters*, **417**, 28–39, https://doi.org/10.1016/j.epsl.2015.02.004.

Lerner, A.H., Wallace, P.J., et al. 2021. The petrologic and degassing behavior of sulfur and other magmatic volatiles from the 2018 eruption of Kīlauea, Hawai'i: melt concentrations, magma storage depths, and magma recycling. *Bulletin of Volcanology*, **83**, 43, https://doi.org/10.1007/s00445-021-01459-y.

Lesne, P., Scaillet, B. and Pichavant, M. 2015. The solubility of sulfur in hydrous basaltic melts. *Chemical Geology*, **418**, 104–116, https://doi.org/10.1016/J.CHEMGEO.2015.03.025.

Li, C. and Ripley, E.M. 2005. Empirical equations to predict the sulfur content of mafic magmas at sulfide saturation and applications to magmatic sulfide deposits. *Mineralium Deposita*, **40**, 218–230, https://doi.org/10.1007/s00126-005-0478-8.

Liggins, P., Shorttle, O. and Rimmer, P.B. 2020. Can volcanism build hydrogen-rich early atmospheres? *Earth and Planetary Science Letters*, **550**, 116546, https://doi.org/10.1016/J.EPSL.2020.116546.

Luhr, J.F. 2008a. Primary igneous anhydrite: Progress since its recognition in the 1982 El Chichón trachyandesite. *Journal of Volcanology and Geothermal Research*, **175**, 394–407, https://doi.org/10.1016/J.JVOLGEORES.2008.02.016.

Luhr, J.F. 2008b. Primary igneous anhydrite: Progress since its recognition in the 1982 El Chichón trachyandesite. *Journal of Volcanology and Geothermal Research*, **175**, 394–407, https://doi.org/10.1016/J.JVOLGEORES.2008.02.016.

Luhr, J.F., Carmichael, I.S.E. and Varekamp, J.C. 1984. The 1982 eruptions of El Chichón Volcano, Chiapas, Mexico: Mineralogy and petrology of the anhydritebearing pumices. *Journal of Volcanology and Geothermal Research*, **23**, 69–108, https://doi.org/10.1016/0377-0273(84)90057-X.

Mathez, E.A. 1984. Influence of degassing on oxidation states of basaltic magmas. *Nature*, **310**, 371–375, https://doi.org/10.1038/310371a0.

Matjuschkin, V., Blundy, J.D. and Brooker, R.A. 2016. The effect of pressure on sulphur speciation in mid- to deep-crustal arc magmas and implications for the formation of porphyry copper deposits. *Contributions to Mineralogy and Petrology*, **171**, 66, https://doi.org/10.1007/s00410-016-1274-4.

Matthews, S.J., Sparks, R.S.J. and Gardeweg, M.C. 1999. The Piedras Grandes-Soncor Eruptions, Lascar Volcano, Chile; Evolution of a Zoned Magma Chamber in the Central Andean Upper Crust. *Journal of Petrology*, **40**, 1891–1919, https://doi.org/10.1093/petroj/40.12.1891.

Métrich, N. 2021. Redox State of Volatiles and Their Relationships with Iron in Silicate Melts. 215–232, https://doi.org/10.1002/9781119473206.CH11.

Métrich, N. and Wallace, P.J. 2009. Volatile Abundances in Basaltic Magmas and Their Degassing Paths Tracked by Melt Inclusions. *Reviews in Mineralogy and Geochemistry*, **69**.

Métrich, N., Berry, A.J., O'Neill, H.S.C. and Susini, J. 2009. The oxidation state of sulfur in synthetic and natural glasses determined by X-ray absorption spectroscopy. *Geochimica et Cosmochimica Acta*, **73**, 2382–2399, https://doi.org/10.1016/J.GCA.2009.01.025.

Moretti, R. 2021. Ionic Syntax and Equilibrium Approach to Redox Exchanges in Melts: Basic

Concepts and the Case of Iron and Sulfur in Degassing Magmas. *In*: Moretti, R. and Neuville, D. R. (eds) *Magma Redox Geochemistry*, *Geophysical Monograph Series*. 115–138., https://doi.org/10.1002/9781119473206.CH6.

Moretti, R. and Ottonello, G. 2003. Polymerization and disproportionation of iron and sulfur in silicate melts: insights from an optical basicity-based approach. *Journal of Non-Crystalline Solids*, **323**, 111–119, https://doi.org/10.1016/S0022-3093(03)00297-7.

Moretti, R. and Ottonello, G. 2005. Solubility and speciation of sulfur in silicate melts: The Conjugated Toop-Samis-Flood-Grjotheim (CTSFG) model. *Geochimica et Cosmochimica Acta*, **69**, 801–823, https://doi.org/10.1016/J.GCA.2004.09.006.

Moretti, R. and Papale, P. 2004. On the oxidation state and volatile behavior in multicomponent gas-melt equilibria. *Chemical Geology*, **213**, 265–280, https://doi.org/10.1016/j.chemgeo.2004.08.048.

Moretti, R., Papale, P. and Ottonello, G. 2003. A model for the saturation of C-O-H-S fluids in silicate melts. *Geological Society, London, Special Publications*, **213**, 81–101, https://doi.org/10.1144/GSL.SP.2003.213.01.06.

Moussallam, Y., Oppenheimer, C., et al. 2014. Tracking the changing oxidation state of Erebus magmas, from mantle to surface, driven by magma ascent and degassing. *Earth and Planetary Science Letters*, **393**, 200–209, https://doi.org/10.1016/j.epsl.2014.02.055.

Moussallam, Y., Edmonds, M., Scaillet, B., Peters, N., Gennaro, M.E., Sides, I. and Oppenheimer, C. 2016. The impact of degassing on the oxidation state of basaltic magmas: A case study of Kīlauea volcano. *Earth and Planetary Science Letters*, **450**, 317–325, https://doi.org/10.1016/j.epsl.2016.06.031.

Moussallam, Y., Longpré, M.-A., et al. 2019. Mantle plumes are oxidised. *Earth and Planetary Science Letters*, **527**, 115798, https://doi.org/10.1016/J.EPSL.2019.115798.

Muth, M.J. and Wallace, P.J. 2021. Slab-derived sulfate generates oxidized basaltic magmas in the southern Cascade arc (California, USA). *Geology*, https://doi.org/10.1130/G48759.1.

Nash, W.M., Smythe, D.J. and Wood, B.J. 2019. Compositional and temperature effects on sulfur speciation and solubility in silicate melts. *Earth and Planetary Science Letters*, **507**, 187–198, https://doi.org/10.1016/J.EPSL.2018.12.006.

Newman, S. and Lowenstern, J.B. 2002. VolatileCalc: a silicate melt–H2O–CO2 solution model written in Visual Basic for excel. *Computers & Geosciences*, **28**, 597–604, https://doi.org/10.1016/S0098-3004(01)00081-4.

O'Neill, H. 2020. The thermodynamic controls on sulfide saturation in silicate melts with application to Ocean Floor Basalts., https://doi.org/10.1002/ESSOAR.10503096.1.

O'Neill, H.S.C. and Mavrogenes, J.A. 2002. The Sulfide Capacity and the Sulfur Content at Sulfide Saturation of Silicate Melts at 1400degreesC and 1 bar. *Journal of Petrology*, **43**, 1049–1087, https://doi.org/10.1093/petrology/43.6.1049.

O'Neill, H.S.C. and Mavrogenes, J.A. 2019. The Sulfate Capacity of Silicate Melts at Atmospheric Pressure. *In*: *Goldschimdt Conference Abstracts*. 2480.

Oppenheimer, C., Scaillet, B. and Martin, R.S. 2011. Sulfur Degassing From Volcanoes: Source Conditions, Surveillance, Plume Chemistry and Earth System Impacts. *Reviews in Mineralogy and Geochemistry*, **73**, 363–421, https://doi.org/10.2138/RMG.2011.73.13.

Papale, P., Moretti, R. and Barbato, D. 2006. The compositional dependence of the saturation surface of H2O+CO2 fluids in silicate melts. *Chemical Geology*, **229**, 78–95, https://doi.org/10.1016/j.chemgeo.2006.01.013.

Parat, F., Holtz, F. and Streck, M.J. 2011. Sulfur-bearing Magmatic Accessory Minerals. *Reviews*

in Mineralogy and Geochemistry, **73**, 285–314, https://doi.org/10.2138/rmg.2011.73.10.
Paris, E., Giuli, G., Carroll, M.R. and Davoli, I. 2001. The valence and speciation of sulfur in glasses by X-ray absorption spectroscopy. *The Canadian Mineralogist*, **39**, 331–339, https://doi.org/10.2113/gscanmin.39.2.331.
Renggli, C.J., King, P.L., Henley, R.W. and Norman, M.D. 2017. Volcanic gas composition, metal dispersion and deposition during explosive volcanic eruptions on the Moon. *Geochimica et Cosmochimica Acta*, **206**, 296–311, https://doi.org/10.1016/J.GCA.2017.03.012.
Rose, W.I., Stoiber, R.E. and Malinconico, L.L. 1982. Eruptive gas compositions and fluxes of explosive volcanoes: Budgets of S and Cl emitted from Fuego volcano, Guatemala. *In*: Thorpe RS (ed.) *Andesites: Orogenic Andesites and Related Rocks*. 669–676.
Rye, R.O., Luhr, J.F. and Wasserman, M.D. 1984. Sulfur and oxygen isotopic systematics of the 1982 eruptions of El Chichón Volcano, Chiapas, Mexico. *Journal of Volcanology and Geothermal Research*, **23**, 109–123, https://doi.org/10.1016/0377-0273(84)90058-1.
Sato, M. 1978. Oxygen fugacity of basaltic magmas and the role of gas-forming elements. *Geophysical Research Letters*, **5**, 447–449, https://doi.org/10.1029/GL005i006p00447.
Sato, M. and Wright, T.L. 1966. Oxygen fugacities directly measured in magmatic gases. *Science*, **153**, 1103–1105, https://doi.org/10.1126/SCIENCE.153.3740.1103.
Scaillet, B. and Pichavant, M. 2003. Experimental constraints on volatile abundances in arc magmas and their implications for degassing processes. *Geological Society, London, Special Publications*, **213**, 23–52, https://doi.org/10.1144/GSL.SP.2003.213.01.03.
Scaillet, B. and Pichavant, M. 2004. Role of fO2 on fluid saturation in oceanic basalt. *Nature 2004 430:6999*, **430**, 1–1, https://doi.org/10.1038/nature02814.
Scaillet, B., Luhr, J. and Carroll, M.R. 2003. Petrological and volcanological constraints on volcanic sulfur emissions to the atmosphere. *Geophysical Monograph - American Geophysical Union*, **139**, 11–40.
Sharma, K., Blake, S., Self, S. and Krueger, A.J. 2004. SO2 emissions from basaltic eruptions, and the excess sulfur issue. *Geophysical Research Letters*, **31**, 13612, https://doi.org/10.1029/2004GL019688.
Shima, H. and Naldrett, A.J. 1975. Solubility of sulfur in an ultramafic melt and the relevance of the system Fe-S-O. *Economic Geology*, **70**, 960–967, https://doi.org/10.2113/gsecongeo.70.5.960.
Shinohara, H. 2008. Excess degassing from volcanoes and its role on eruptive and intrusive activity. *Reviews of Geophysics*, **46**, https://doi.org/10.1029/2007RG000244.
Smythe, D.J., Wood, B.J. and Kiseeva, E.S. 2017. The S content of silicate melts at sulfide saturation: New experiments and a model incorporating the effects of sulfide composition. *American Mineralogist*, **102**, 795–803, https://doi.org/10.2138/AM-2017-5800CCBY.
Stoiber, R.E. and Jepsen, A. 1973. Sulfur dioxide contributions to the atmosphere by volcanoes. *Science*, **182**, 577–578, https://doi.org/10.1126/SCIENCE.182.4112.577.
Thordarson, T., Self, S., Óskarsson, N. and Hulsebosch, T. 1996. Sulfur, chlorine, and fluorine degassing and atmospheric loading by the 1783–1784 AD Laki (Skaftár Fires) eruption in Iceland. *Bulletin of Volcanology 1996 58:2*, **58**, 205–225, https://doi.org/10.1007/S004450050136.
Tomkins, A.G., Rebryna, K.C., Weinberg, R.F. and Schaefer, B.F. 2012. Magmatic Sulfide Formation by Reduction of Oxidized Arc Basalt. *Journal of Petrology*, **53**, 1537–1567, https://doi.org/10.1093/petrology/egs025.
Venugopal, S., Schiavi, F., Moune, S., Bolfan-Casanova, N., Druitt, T. and Williams-Jones, G.

2020. Melt inclusion vapour bubbles: the hidden reservoir for major and volatile elements. *Scientific Reports*, **10**, 9034, https://doi.org/10.1038/s41598-020-65226-3.

Vidal, C.M., Métrich, N., et al. 2016. The 1257 Samalas eruption (Lombok, Indonesia): the single greatest stratospheric gas release of the Common Era. *Scientific Reports 2016 6:1*, **6**, 1–13, https://doi.org/10.1038/srep34868.

Wallace, P.J. 2001. Volcanic SO2 emissions and the abundance and distribution of exsolved gas in magma bodies. *Journal of Volcanology and Geothermal Research*, **108**, 85–106, https://doi.org/10.1016/S0377-0273(00)00279-1.

Wallace, P.J. 2005. Volatiles in subduction zone magmas: concentrations and fluxes based on melt inclusion and volcanic gas data. *Journal of Volcanology and Geothermal Research*, **140**, 217–240, https://doi.org/10.1016/j.jvolgeores.2004.07.023.

Wallace, P.J. and Carmichael, I.S.E. 1994. S speciation in submarine basaltic glasses as determined by measurements of SKa X-ray wavelength shifts. *American Mineralogist*, **79**, 161–167.

Wallace, P.J. and Edmonds, M. 2011. The Sulfur Budget in Magmas: Evidence from Melt Inclusions, Submarine Glasses, and Volcanic Gas Emissions. *Reviews in Mineralogy and Geochemistry*, **73**, 215–246, https://doi.org/10.2138/rmg.2011.73.8.

Wallace, P.J. and Gerlach, T.M. 1994. Magmatic vapor source for sulfur dioxide released during volcanic eruptions: Evidence from Mount Pinatubo. *Science*, **265**, 497–499, https://doi.org/10.1126/SCIENCE.265.5171.497.

Wetzel, D.T., Hauri, E.H., Saal, A.E. and Rutherford, M.J. 2015. Carbon content and degassing history of the lunar volcanic glasses. *Nature Geoscience 2015 8:10*, **8**, 755–758, https://doi.org/10.1038/ngeo2511.

Wilke, M., Klimm, K. and Kohn, S.C. 2011. Spectroscopic studies on sulfur speciation in synthetic and natural glasses. *Reviews in Mineralogy and Geochemistry*, **73**, 41–78, https://doi.org/10.2138/rmg.2011.73.3.

Zajacz, Z. and Tsay, A. 2019. An accurate model to predict sulfur concentration at anhydrite saturation in silicate melts. *Geochimica et Cosmochimica Acta*, **261**, 288–304, https://doi.org/10.1016/J.GCA.2019.07.007.

Zajacz, Z., Candela, P.A., Piccoli, P.M. and Sanchez-Valle, C. 2012. The partitioning of sulfur and chlorine between andesite melts and magmatic volatiles and the exchange coefficients of major cations. *Geochimica et Cosmochimica Acta*, **89**, 81–101, https://doi.org/10.1016/J.GCA.2012.04.039.

Zolotov, M.Y. and Fegley, B. 2000. Eruption conditions of Pele Volcano on Io inferred from chemistry of its volcanic plume. *Geophysical Research Letters*, **27**, 2789–2792, https://doi.org/10.1029/2000GL011608.

Tables

Table 1 Summary of the relationships [$Z \propto (f_{O2})^a(Y)^b$] and slopes between independent (Y) and dependent (Z) variables when T and f_{O2} are always independent variables for silicate melt + vapour.

Z	Y = f_{S2}				Y = w^m_{ST}				Y = P			
	a	b	ς	σ	a	b	ς	σ	a	b	ς	σ
Silicate melt ≅ S^{2-} and vapour ≅ S_2 (purple)												
f_{S2}	**0.0**	**+1.0**	**0.0**	**0.0**	+1.0	+2.0	+1.0	-0.5	0.0	+1.0	0.0	0.0
f_{SO2}	+1.0	+0.5	+1.0	-2.0	+1.5	+1.0	+1.5	-1.5	+1.0	+0.5	+1.0	-2.0
P (≅ p_{S2} ≅ f_{S2})	0.0	+1.0	0.0	0.0	+1.0	+2.0	+1.0	-0.5	**0.0**	**+1.0**	**0.0**	**0.0**
w^m_{S2-}	-0.5	+0.5	-0.5	+1.0	0.0	+1.0	0.0	0.0	-0.5	+0.5	-0.5	+1.0
w^m_{S6+}	+1.5	+0.5	+1.5	-3.0	+2.0	+2.0	+2.0	-1.0	+1.5	+0.5	+1.5	-3.0
w^m_{ST} (≅ w^m_{S2-})	-0.5	+0.5	-0.5	+1.0	**0.0**	**+1.0**	**0.0**	**0.0**	-0.5	+0.5	-0.5	+1.0
Silicate melt ≅ S^{2-} and vapour ≅ SO_2 (turquoise)												
f_{S2}	**0.0**	**+1.0**	**0.0**	**0.0**	+1.0	+2.0	+1.0	-0.5	-2.0	+2.0	-2.0	+1.0
f_{SO2}	+1.0	+0.5	+1.0	-2.0	+1.5	+1.0	+1.5	-1.5	0.0	+1.0	0.0	0.0
P (≅ p_{SO2} ≅ f_{SO2})	+1.0	+0.5	+1.0	-2.0	+1.5	+1.0	+1.5	-1.5	**0.0**	**+1.0**	**0.0**	**0.0**
w^m_{S2-}	-0.5	+0.5	-0.5	+1.0	0.0	+1.0	0.0	0.0	-1.5	+1.0	-1.5	+1.5
w^m_{S6+}	+1.5	+0.5	+1.5	-3.0	+2.0	+2.0	+2.0	-1.0	+0.5	+1.0	+0.5	-0.5
w^m_{ST} (≅ w^m_{S2-})	-0.5	+0.5	-0.5	+1.0	**0.0**	**+1.0**	**0.0**	**0.0**	-1.5	+1.0	-1.5	+1.5
Silicate melt ≅ S^{6+} and vapour ≅ SO_2 (yellow)												
f_{S2}	**0.0**	**+1.0**	**0.0**	**0.0**	-3.0	+2.0	-3.0	+1.5	-2.0	+2.0	-2.0	+1.0
f_{SO2}	+1.0	+0.5	+1.0	-2.0	-0.5	+1.0	-0.5	+0.5	0.0	+1.0	0.0	0.0
P (≅ p_{SO2} ≅ f_{SO2})	+1.0	+0.5	+1.0	-2.0	-0.5	+1.0	-0.5	+0.5	**0.0**	**+1.0**	**0.0**	**0.0**
w^m_{S2-}	-0.5	+0.5	-0.5	+1.0	-2.0	+1.0	-2.0	-2.0	-1.5	+1.0	-1.5	+1.5
w^m_{S6+}	+1.5	+0.5	+1.5	-3.0	0.0	+1.0	0.0	0.0	+0.5	+1.0	+0.5	-0.5
w^m_{ST} (≅ w^m_{S6+})	+1.5	+0.5	+1.5	-3.0	**0.0**	**+1.0**	**0.0**	**0.0**	+0.5	+1.0	+0.5	-0.5

Notes: Derivations are in the Supplementary Material. The slopes of $\log_{10}(Y)$ vs. $\log_{10}(Z)$ are given as ς when Y is constant (slopes of Z-curves in Figure 2) and σ when Y varies (slopes of Z-contours in Figures 3–5). $p_i \cong f_i$ because $\gamma_i \sim 1$. **Bold** indicates the independent variable (Y). For example, when the silicate melt is S^{2-}-dominated and the vapour is S_2-dominated in the purple region (first group of f_{S2}-f_{SO2}-P-w^m_{S2-}-w^m_{S6+}-w^m_{ST} horizontally) and $Y = f_{S2}$ (first group of a-b-ς-σ vertically), the slope of w^m_{S6+} when f_{S2} is constant (ς) is +1.5 (Figure 2a) and the slope of the contours (σ) of $Z = w^m_{ST}$ are -(-0.5)/(0.5) = +1.0 (Figure 3c).

Figure Captions

Figure 1 Schematic figures of sulfur in magmatic and volcanic systems. In all panels, silicate melt is shown in pink, vapour in blue, sulfide melt in yellow, and anhydrite in grey. (a) Ternary diagram of the idealised silicate-S_2-O_2 system used in this study, which contains silicate melt and vapour. The vapour is constrained to the S_2-O_2 binary, which includes S_2, O_2, and SO_2 as species. An example tie-line between the composition of the silicate melt and vapour (including the composition of the bulk system) is shown by the black line. Sulfide melt and anhydrite lie outside this ternary. (b) Schematic illustration of the interplay between the different species in the silicate melt, which contains S^{2-}, SO_4^{2-}, FeO, and $FeO_{1.5}$; vapour, which contains S_2, O_2, and SO_2; sulfide melt, which contains S^{2-}; and anhydrite, which contains SO_4^{2-}. Phases and species that dominate under reducing conditions are to the left, whilst those that dominate under oxidising conditions are to the right. Two-way arrows indicate species that can interact within, and between different, phases. (c) Illustration showing the involvement of sulfur in different magmatic and volcanic processes. In detail, the process and techniques influenced by the sulfur solubility minimum (SS^{min}, left) and maximum (SS^{max}, right) are highlighted from "Implications of SSmin and SSmax for magmatic and volcanic processes". SS^{min}, where silicate melt + vapour are stable, effects the gas release from magma mixing and crustal assimilation ("Magma mixing and crustal assimilation"), degassing depth ("Magma ascent and degassing"), and the f_{O2} of surface gas emissions ("Magma ascent and degassing"), as well as causing P^{v}_{sat} to be underestimated ("Magma ascent and degassing") and affecting the reliability of the petrologic method ("Volcanic emissions"). SS^{max}, where silicate melt + vapour + sulfide melt + anhydrite are stable, sets the maximum S content of partial mantle melts ("Mantle melting") and is a common feature of large SO_2 emissions from explosive eruptions ("Volcanic emissions"). It also effects the reliability of the petrologic method ("Volcanic emissions") and can be utilised as an oxybarometer from w^{m}_{ST} measurements ("Using *wmST* as an oxybarometer"). *Abbreviations: sil*^{m}, silicate melt; *v*, vapour; *sulf*^{m}, sulfide melt; *anh*, anhydrite; P^{v}_{sat}, pressure of vapour-saturation; f_{O2}, oxygen fugacity; w^{m}_{ST}, total dissolved S content of the silicate melt.

Figure 2 Different dependent variables (*Z*) versus oxygen fugacity (f_{O2}) relative to the Fayalite-Magnetite-Quartz (FMQ) buffer (shown as ΔFMQ) for silicate melt + vapour: (a, c, e) concentration of dissolved S-bearing species in the silicate melt (w^{m}_{i}), where *i* = total sulfur (S_T, white solid), sulfide (S^{2-}, black dot), or sulfate (S^{6+}, black dash); and (b, d, f) pressure (*P*, white solid) or partial pressure (p_i), where *i* = sulfur (S_2, black dot), sulfur dioxide (SO_2, black dash), or oxygen (O_2, black dot dash). In each column a different independent variable (*Y*) is fixed (indicated by the horizontal line in either the top or bottom row): (a–b) $f_{S2} = 10^{-4}$ bar; (c–d) $w^{m}_{ST} = 400$ ppm; and (e–f) $P = 1$ bar. The background colour indicates the S speciation of the silicate melt and vapour, where boundaries are defined at $[S^{6+}/S_T]^m = 0.1$ and 0.9 ($[S^{2-}]^m$ where $[S^{6+}/S_T]^m < 0.1$, $[S^{2-}+S^{6+}]^m$ where $0.1 \leq [S^{6+}/S_T]^m \leq 0.9$, and $[S^{6+}]^m$ where $[S^{6+}/S_T]^m > 0.9$) and $x^{v}_{SO2} = 0.1$ or 0.9 ($[S_2]^v$ where $x^{v}_{SO2} < 0.1$, $[S_2+SO_2]^v$ where $0.1 \leq x^{V}_{SO2} \leq 0.9$, or $[SO_2]^v$ where $x^{v}_{SO2} > 0.9$): purple = $[S^{2-}]^m+[S_2]^v$; blue = $[S^{2-}]^m+[S_2+SO_2]^v$; turquoise = $[S^{2-}]^m+[SO_2]^v$; green = $[S^{2-}+S^{6+}]^m+[SO_2]^v$; and yellow = $[S^{6+}]^m+[SO_2]^v$. The vertical grey lines show where sulfide melt (solid) or anhydrite (dashed) would saturate. Slopes (ς) are labelled in boxes outlined in black. α (in panels b, d, and f) indicates when $p_{O2} = p_{S2}$, and β in panel (d) indicates a change in slope of *P* from $\varsigma = +1$ to +1.5 with increasing f_{O2}. Note that to the right of α in (b) that $\gamma_{S2} = 2.14$ at $P = 4507$ bar, causing p_{S2} to deviate noticeably from f_{S2}, just visible as the slight downturn in the black dotted curve at high f_{O2}. *Abbreviations: sil*^{m}, silicate melt; *v*, vapour; *sulf*^{m}, sulfide melt; and *anh*, anhydrite.

Figure 3 Sulfur fugacity ($Y = f_{S2}$) versus oxygen fugacity (f_{O2}) for silicate melt + vapour at T = 1200 °C. Contours of Z are shown for: (a) sulfur dioxide fugacity (f_{SO2}); (b) pressure (P), and (c) total S content of the silicate melt (w^m_{ST}). (d) Sulfur speciation of the vapour (S_2 and/or SO_2) and silicate melt (S^{2-} and/or S^{6+}), where boundaries are defined for the vapour at x^v_{SO2} = 0.1 or 0.9 (black dashed curves) and for the silicate melt at $[S^{6+}/S_T]^m$ = 0.1 and 0.9 (black solid curves): purple = $[S^{2-}]^m$+$[S_2]^v$; blue = $[S^{2-}]^m$+$[S_2+SO_2]^v$; turquoise = $[S^{2-}]^m$+$[SO_2]^v$; green = $[S^{2-}+S^{6+}]^m$+$[SO_2]^v$; yellow = $[S^{6+}]^m$+$[SO_2]^v$, light turquoise with black arrow = $[S^{2-}+S^{6+}]^m$+$[S_2+SO_2]^v$ (as in silm, silicate melt; *v*, vapour; *sulf*^{m}, sulfide melt; *anh*, anhydrite; P^v_{sat}, pressure of vapour-saturation; f_{O2}, oxygen fugacity; w^m_{ST}, total dissolved S content of the silicate melt.

Figure 2, although the light turquoise section was not previously intersected). (e) Paths followed in f_{O2}-f_{S2} space for different processes (overlain on contours of $Z = w^m_{ST}$): dark turquoise is constant $f_{S2} = 10^{-4}$ bar (silm, silicate melt; *v*, vapour; *sulf*^{m}, sulfide melt; *anh*, anhydrite; P^v_{sat}, pressure of vapour-saturation; f_{O2}, oxygen fugacity; w^m_{ST}, total dissolved S content of the silicate melt.

*Figure 2*a–b); purple is constant w^m_{ST} = 400 ppm (silm, silicate melt; *v*, vapour; *sulf*^{m}, sulfide melt; *anh*, anhydrite; P^v_{sat}, pressure of vapour-saturation; f_{O2}, oxygen fugacity; w^m_{ST}, total dissolved S content of the silicate melt.

*Figure 2*c–d); blue is constant P = 1 bar (silm, silicate melt; *v*, vapour; *sulf*^{m}, sulfide melt; *anh*, anhydrite; P^v_{sat}, pressure of vapour-saturation; f_{O2}, oxygen fugacity; w^m_{ST}, total dissolved S content of the silicate melt.

*Figure 2*e–f); yellow, green, and light turquoise are constant bulk O_2 = 3.26, 3.87, and 4.23 wt%, respectively (

Figure *8*); and grey is constant μ_{FeS} and/or μ_{CaSO4} equal to sulfide melt- and anhydrite-saturation, respectively (

Figure *6*a–b). In the white region at very low and very high f_{O2} and high f_{S2}, w^m_{ST} > 10 wt% and hence calculations are terminated. The value of the slopes of the curves and contours (σ) are labelled in boxes with a thick black outline. The grey curve indicates the boundary above which silicate melt + vapour is metastable, which is solid when sulfide melt would saturate, dashed when anhydrite would saturate, and the grey star indicates the silicate melt is multiply-saturated with vapour, sulfide melt, and anhydrite. The f_{O2} for different tectonic settings from Cottrell et al. (2021) is shown by horizonal blue bars (extent of the bar shows the range and black vertical line shows the mode) for mid-ocean ridge (light blue), ocean island (intermediate blue), and arc (dark blue) basalts. *Abbreviations: sil*^{m}, silicate melt; *v*, vapour; *sulf*^{m}, sulfide melt; *anh*, anhydrite; MORB, mid-ocean ridge basalts; OIB, ocean island basalts; and Arc, arc basalts.

Figure 4 Total S content of the silicate melt ($Y = w^m_{ST}$) versus oxygen fugacity (f_{O2}) for silicate melt + vapour at T = 1200 °C. Contours of Z are shown for: (a) sulfur fugacity (f_{S2}); (b) sulfur dioxide fugacity (f_{SO2}); and (c) pressure (P). (d) Sulfur speciation of the silicate melt and vapour. (e) Paths followed in f_{O2}-f_{S2} space for different processes (overlain on contours of $Z = P$). See

Figure *3* for details of the coloured regions, different curves, annotations, abbreviations, and f_{O2} ranges. *Note:* anhydrite is not stable at these w^m_{ST} and therefore *anh* does not appear.

Figure 5 Pressure ($Y = P$) versus oxygen fugacity (f_{O2}) at T = 1200 °C for (a–e) silicate melt + vapour and (f–g) silicate melt + (vapour and/or sulfide melt and/or anhydrite) (indicated using *).

Contours of Z are shown for: (a) sulfur fugacity (f_{S2}); (b) sulfur dioxide fugacity (f_{SO2}); and (c, g) total S content of the silicate melt (w^m_{ST}). (d, f) Sulfur speciation of the silicate melt and vapour. In the vapour-undersaturated region of (f): dark grey indicates S^{2-}-dominated silicate melt + sulfide melt; medium grey indicated silicate melt (both S^{2-} and S^{6+} in similar concentrations) and sulfide melt; and light grey indicates S^{6+}-dominated silicate melt + anhydrite. (e, g) Paths followed in f_{O2}-f_{S2} space for different processes (overlain on contours of $Z = w^m_{ST}$). In the white region at high f_{O2} and low P, calculations are unfeasible as $x^v_{O2} > 1$. See

Figure *3* for details of the coloured regions, different curves, annotations, abbreviations, and f_{O2} ranges. *Note:* the blue horizontal dotted and dashed lines in (g) are the P = 200 and 2000 bar, respectively, slices shown in

Figure *6*c–f.

Figure 6 (a, c, e) Total S content of the silicate melt (w^m_{ST}) and (b, d, f) pressure (P) versus oxygen fugacity (f_{O2}) against at T = 1200 °C. When the silicate melt is vapour-saturated, the background is coloured (no vapour is present in the white regions) and the silicate melt and vapour speciation are shown by the background colour (see

Figure *3* for details). Grey or black solid curves indicate sulfide melt-saturation and dashed curves indicate anhydrite-saturation. (a–b) Silicate melt + vapour + (sulfide melt and/or anhydrite) with independent variables of T, f_{O2}, and μ_{FeS} and/or μ_{CaSO4}. At the grey star, both sulfide melt and anhydrite are saturated; hence, both μ_{FeS} and μ_{CaSO4} are specified and f_{O2} is no longer independent. The white horizontal lines and annotations (α, β, and γ) are for the melt inclusion example containing 400 (solid), 3000 (dash), and 13000 (dot) ppm S_T described in "Using *wmST* as an oxybarometer". (c–d) Vapour-undersaturated silicate melt + (sulfide melt and/or anhydrite) with independent variables of T, f_{O2}, P, and μ_{FeS} and/or μ_{CaSO4}; when both μ_{FeS} and μ_{CaSO4} are specified, f_{O2} or P is no longer independent. Silicate melt speciation is indicated by the green vertical lines ($[S^{6+}/S_T]^m$ = 0.1 or 0.9): $[S^{2-}]^m$ at low f_{O2}, $[S^{2-}+S^{6+}]^m$ at intermediate f_{O2}, and $[S^{6+}]^m$ at high f_{O2}. At the vertical grey line, both sulfide melt and anhydrite are saturated. (e–f) Silicate melt + (vapour and/or sulfide melt and/or anhydrite) with independent variables of T, f_{O2}, P, and μ_{FeS} and/or μ_{CaSO4}; when both μ_{FeS} and μ_{CaSO4} are specified, f_{O2} or P is no longer independent. The green vertical line indicates the boundary between $[S^{2-}]^m$ (lower f_{O2}) and $[S^{2-}+S^{6+}]^m$ (higher f_{O2}) when vapour is *not* present ($[S^{6+}/S_T]^m$ = 0.1). At the solid grey vertical line, sulfide melt + vapour are saturated; along the dotted segment, vapour is saturated; and at the dashed grey vertical line, vapour + anhydrite are saturated. Annotations (δ, ε, and ζ) indicate maxima and minima described in "Silicate melt + (vapour and/or sulfide melt and/or anhydrite)". f_{O2} ranges are shown as described in

Figure *3*. *Abbreviations: sil*^{m}, silicate melt; *v*, vapour; *sulf*^{m}, sulfide melt; *anh*, anhydrite; MORB, mid-ocean ridge basalts; OIB, ocean island basalts; and Arc, arc basalts.

Figure 7 Closed-system degassing: pressure (P) versus bulk O_2 content of the system for silicate melt + vapour at T = 1200 °C with a bulk S content of 5000 ppm. Contours of Z are shown for: (a) sulfur fugacity (f_{S2}); (b) sulfur dioxide fugacity (f_{SO2}); (c) total S content dissolved in the silicate melt (w^m_{ST}); (d) oxygen fugacity (f_{O2}); (e) total vapour content of the system (w^v_T) – this includes both S and O in the vapour and hence can exceed 0.5 wt%. (f) Sulfur speciation of the silicate melt and vapour. (g) Paths followed in P-bulk O_2 space for closed-system degassing and the white circle and square connected by a black-long dashed-horizontal line is the mixing example described in "Magma mixing and crustal assimilation" (overlain on contours of $Z = w^m_{ST}$). The solid black

curve is equal to the 5000 ppm w^m_{ST} contour and P^v_{sat}, and $^{SSmin}f_{O2}$ is indicated by a white diamond. The bulk O_2 ranges shown below each figure correspond to the f_{O2} by tectonic setting bars in other figures at P^v_{sat}. See Figure *3* for details of the coloured regions, different curves, annotations, and abbreviations. *Note:* anhydrite is not stable at these conditions and therefore *anh* does not appear.

Figure 8 Closed (solid) and open (black dash) -system depressurisation paths for silicate melt + vapour at T = 1200 °C: (a) sulfur fugacity (f_{S2}); (b) oxygen fugacity (f_{O2}); and (c) total S content dissolved in the silicate melt (w^m_{ST}). Three initial bulk compositions are used, as shown on Figure 7g: 3.26 (yellow), 3.87 (green), and 4.23 (turquoise) wt% O_2.

Figure 9 Pressure of vapour-saturation (P^v_{sat}) versus oxygen fugacity (f_{O2}) for a Hawaiian basaltic melt + vapour at 1200 °C containing different w^m_{ST}: 400 (solid), 2000 (dash), and 5000 (dot) ppm. The background colour indicates the speciation of the silicate melt and vapour and the bars indicate f_{O2} of different tectonic settings (see Figure *3* for details).

Figures

Figure 1

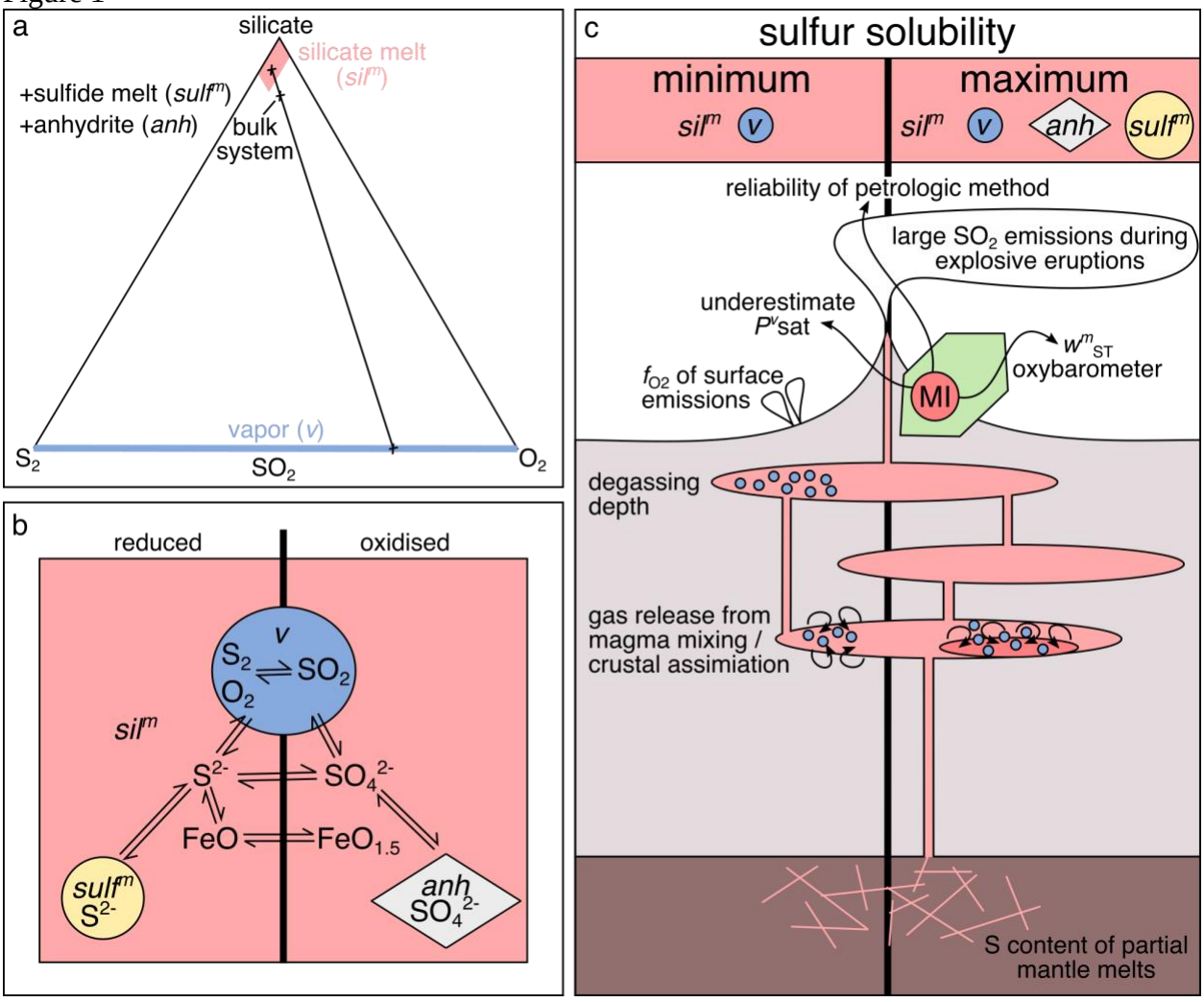

1667 Figure 2

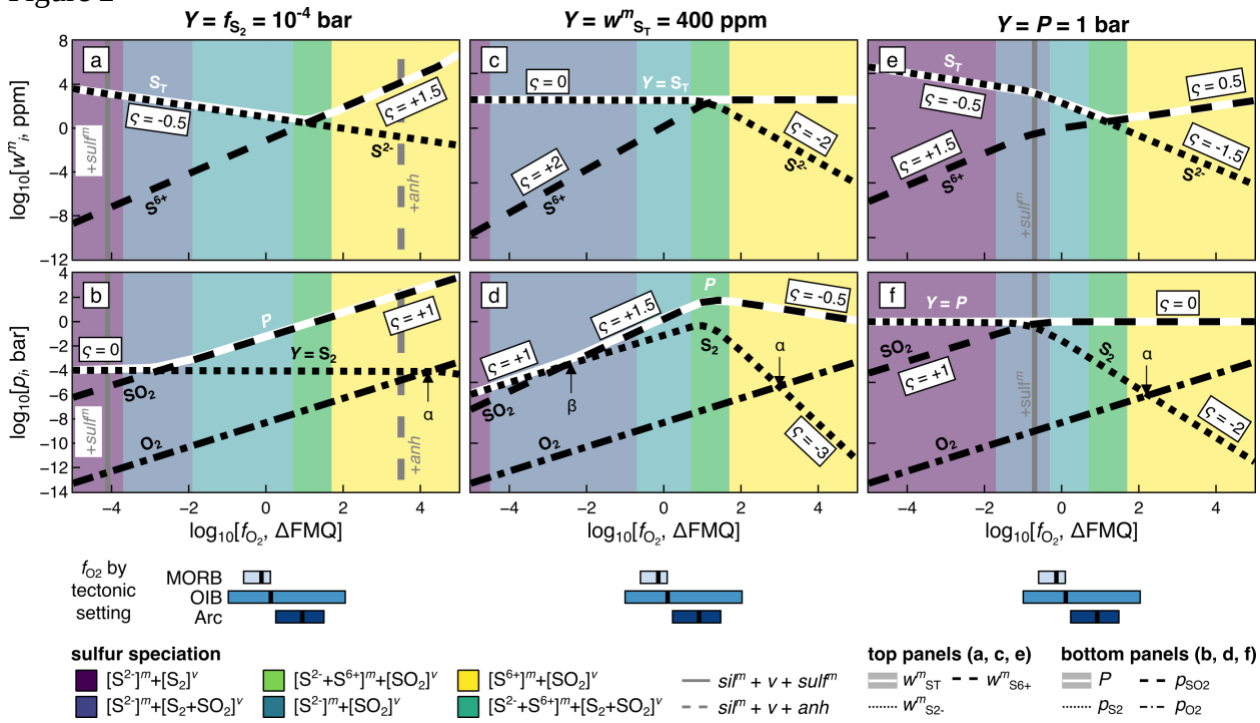

1668

1669 Figure 3

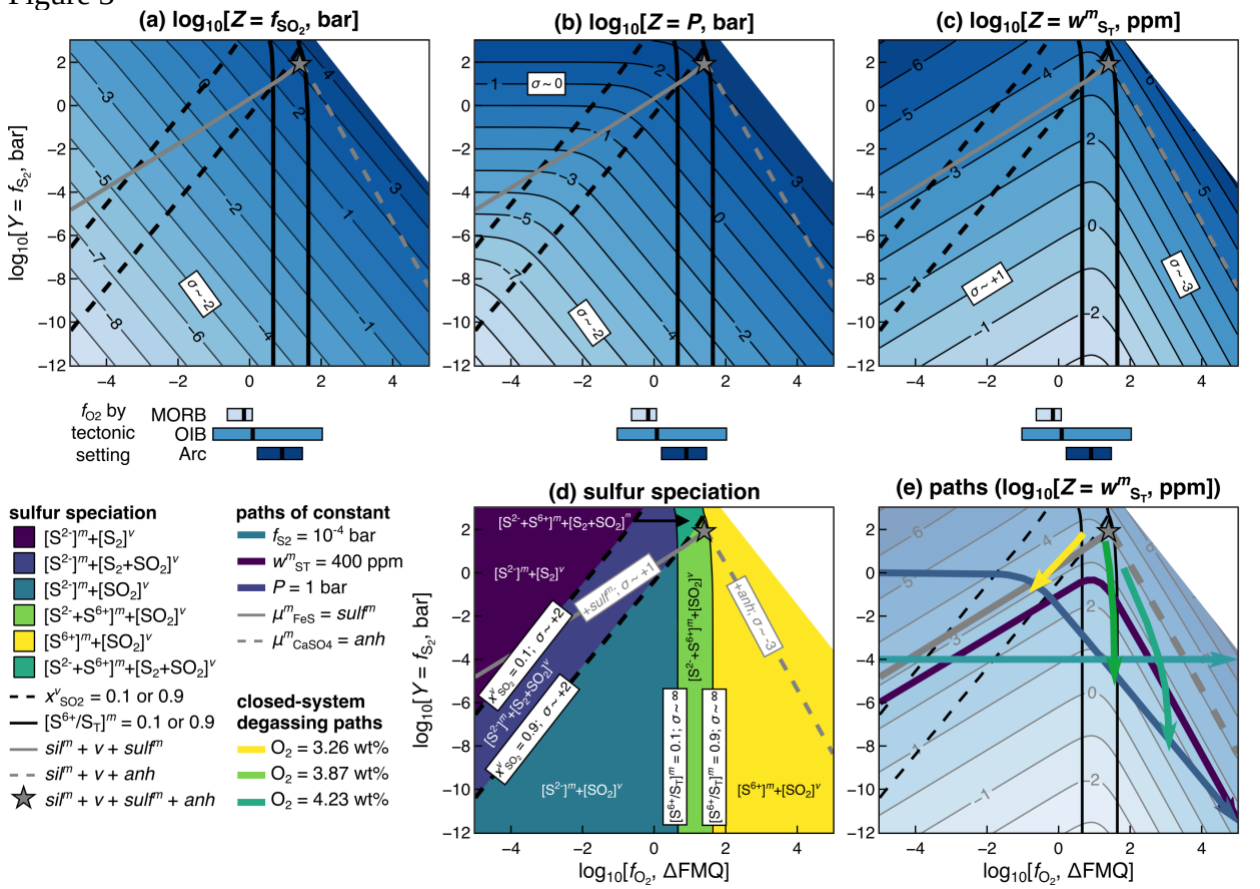

1670
1671

1672 Figure 4

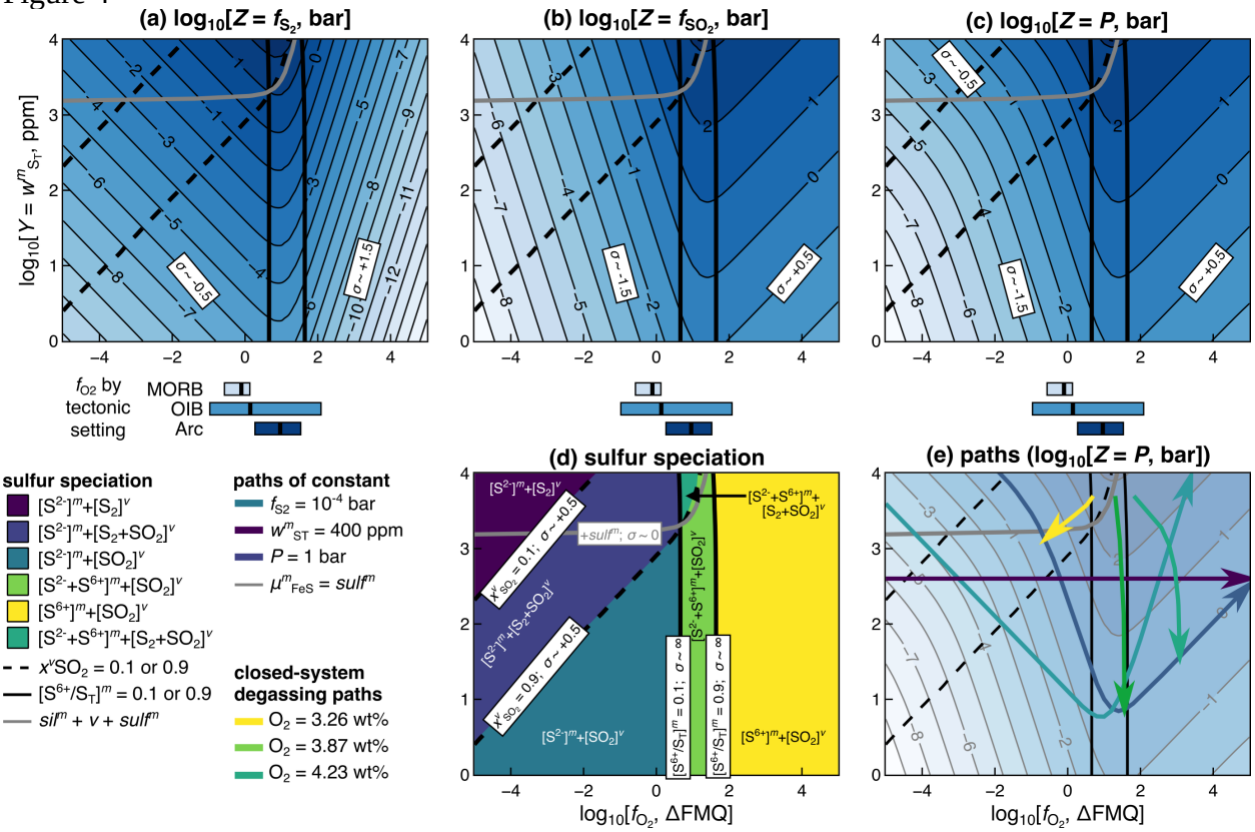

1673

1674 Figure 5

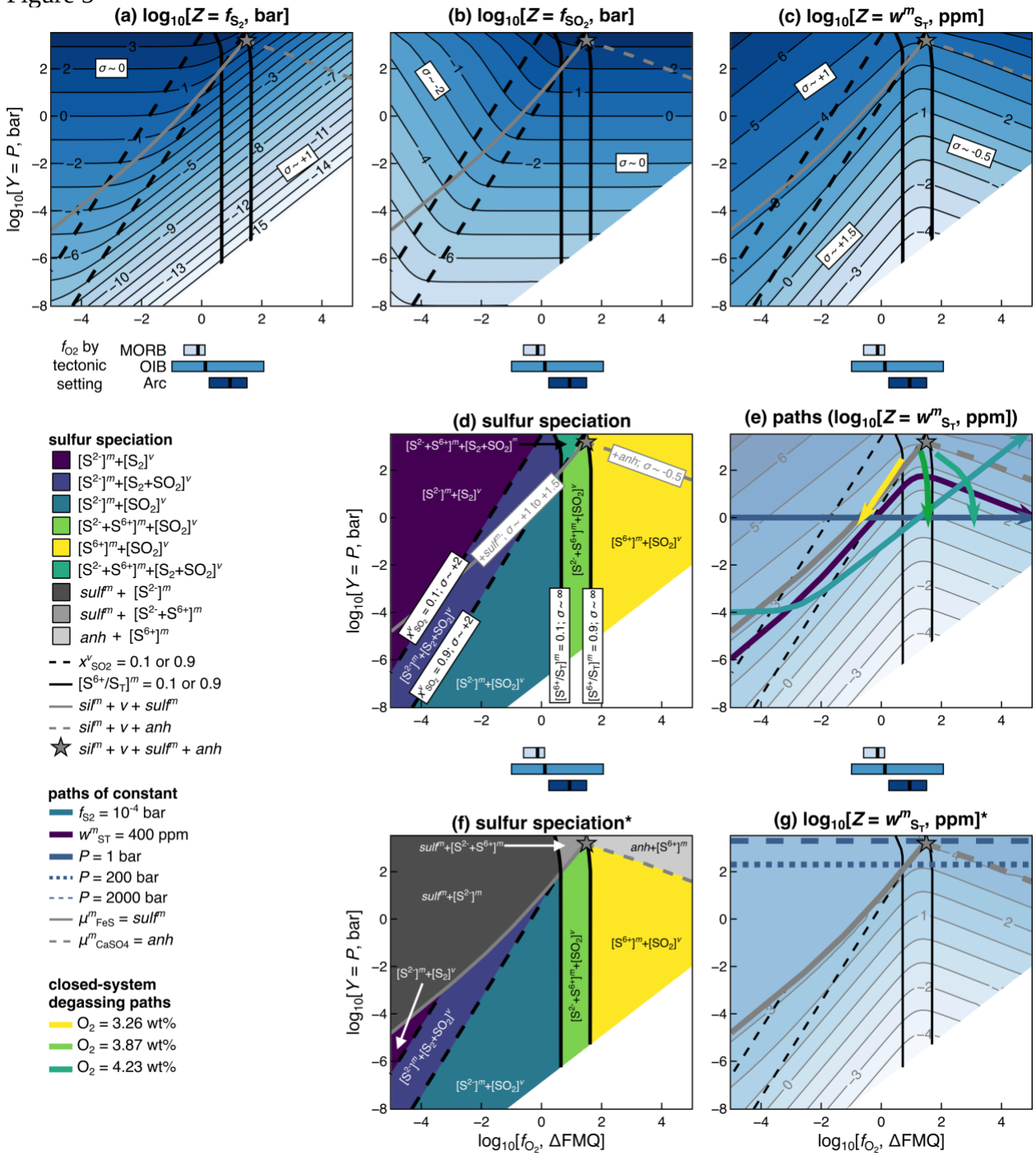

1675

1676 Figure 6

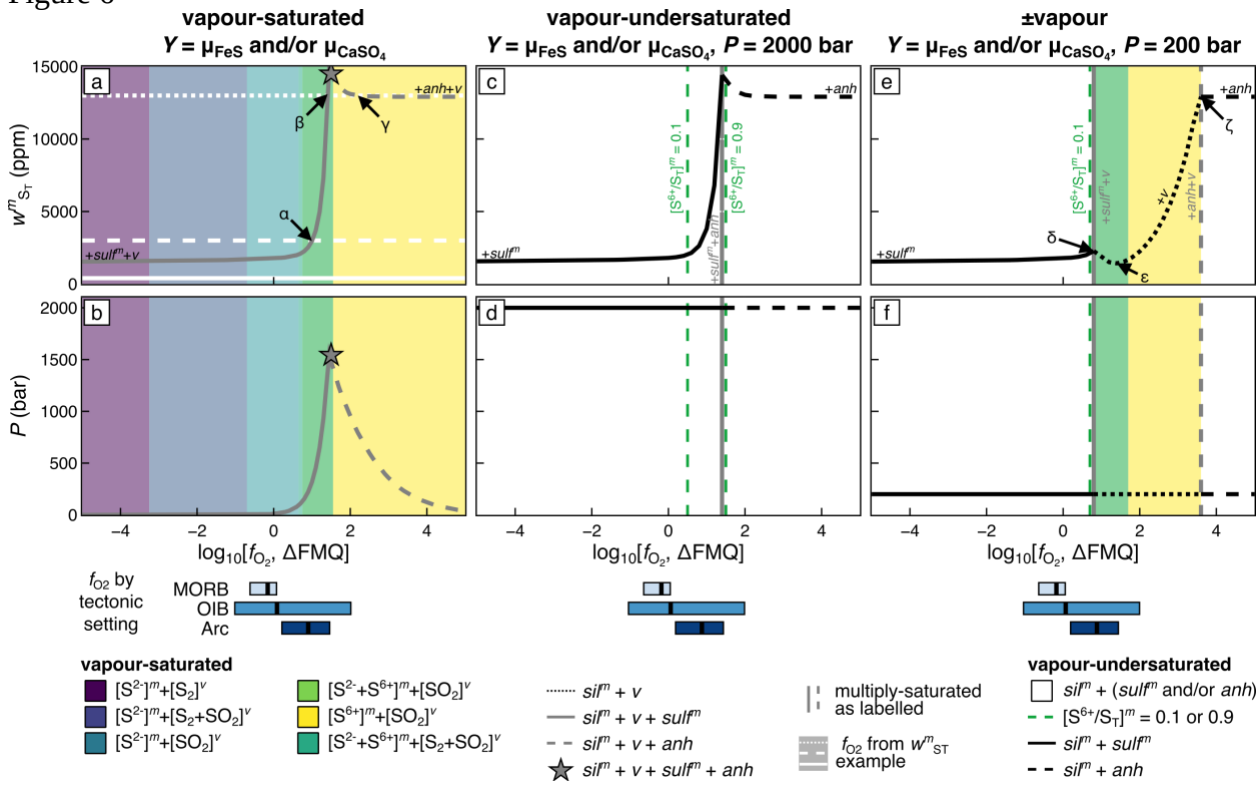

1677

1678 Figure 7

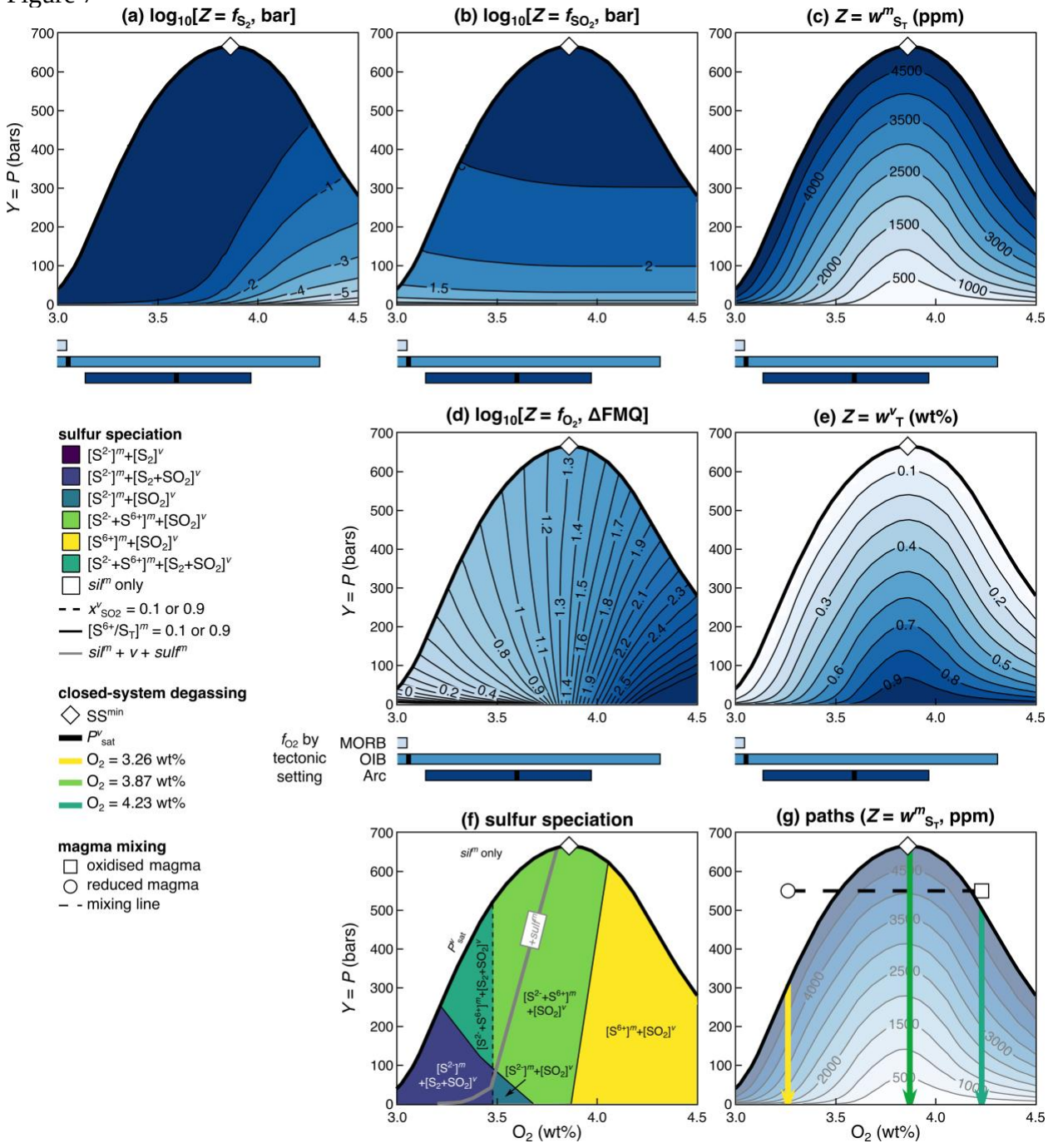

1679

1680 Figure 8

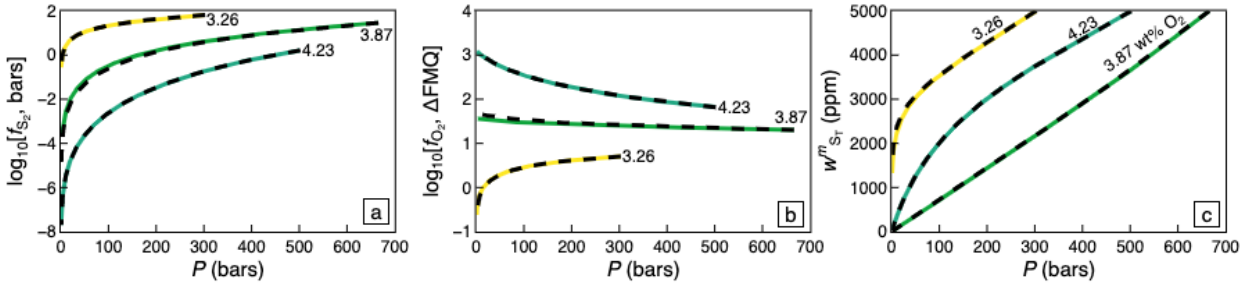

1681

1682 Figure 9

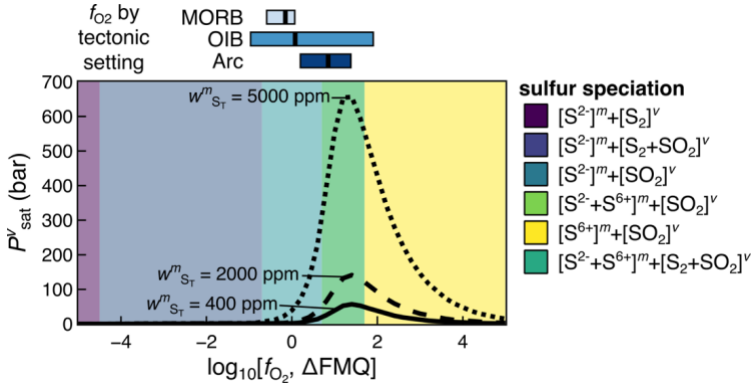

1683